

**Modeling and imaging with the scalar generalized-screen
algorithms in isotropic media**

JÉRÔME H. LE ROUSSEAU

AND

MAARTEN V. DE HOOP

Center for Wave Phenomena, Colorado School of Mines, Golden CO, USA

September 24, 1999

ABSTRACT

The phase-screen and the split-step Fourier methods, which allow modeling and migration in laterally heterogeneous media, are generalized here so as to increase their accuracies for media with large and rapid lateral variations. The medium is defined in terms of a background medium and a perturbation. Such a contrast formulation induces a series expansion of the vertical slowness in which we recognize the first term as the split-step Fourier approximation and the addition of higher-order terms of the expansion increases the accuracy. Employing this expansion in the one-way scalar propagator yields the scalar one-way generalized-screen propagator. We also introduce a generalized-screen representation of the reflection operator. The interaction between the up- and downgoing fields is taken into account by a Bremmer series. These results are then cast into numerical algorithms. We analyze the accuracy of the generalized-screen method in complex structures using synthetic models that exhibit significant multi-pathing: the IFP 2D Marmousi model and the SEG-EAGE 3D salt model. Wide-angle propagation is better handled with the generalized-screen methods than with the split-step Fourier method. As a result, the generalized-screen approach yields better imaging in complex structures.

INTRODUCTION

In realistic geological models, heterogeneity in medium properties is such that the phenomenon of multiple scattering is significant. We distinguish two classes of multiple scattering: one in which the multiples are identified with respect to the projection of their propagation paths onto the *vertical* direction (depth), and one where the multiples are identified with respect to the projection of their propagation paths onto the *horizontal* plane. In the asymptotic framework of wavefront analysis, paths are rays. The *first* class of multiple scattering is associated with ‘turning rays’ and ‘internal multiples’ as well as ‘surface multiples’, the *second*, possibly combined with the first class of multiple scattering, is associated with ‘multi-pathing’.

Seismic imaging and inversion are now commonly applied to regions where geologic complexities are present. An important part of the seismic energy is not contained in the ‘first’ arrival. An accurate prediction of multi-pathing and ‘second’ arrivals is the key to a better processing. A ray-theoretic treatment of the multi-pathing is not straightforward and is algorithmically rather involved (De Hoop & Brandsberg-Dahl, 1999). Wave extrapolation methods are able to predict multi-pathing (second class of multiple scattering), with no need to follow the formation of caustics explicitly. Also, with 3D surveys becoming standard practice, fast 3D algorithms are in demand. On the one hand, the full 3D extension of finite-difference methods is costly and restrict their application. On the other hand, methods such as the phase-screen (Ratcliffe, 1956) and the closely related split-step Fourier (Stoffa *et al.*, 1990) methods yield a faster 3D algorithm. They are, however, limited in their capacity to predict large-angle propagation where significant lateral heterogeneities are present. Because of their attractive properties (3D, multi-pathing), we propose, here, to generalize this latter family of algorithms, enhancing their accuracy. Since this algorithmic structure coincides with the one of the classical phase-screen propagator, we denote our approximations as generalized screens (GS). Also, we propose to predict the first class of multiple scattering by the introduction of the Bremmer series (De Hoop, 1996).

Our approach accounts for the *first* class of multiple scattering through use of the generalized Bremmer series (De Hoop, 1996), and for the *second* class of multi-pathing by means of the GS propagation (De Hoop *et al.*, 1999).

A scattering theory that follows the ray picture but accounts for full-wave behavior has been developed by De Hoop (1996). It is based on an extension of the Bremmer coupling series to multi-dimensionally varying media. Bremmer's method decomposes the wavefield into a recursion of one-way propagation operators each using the previous wavefield as a source. Thus, the method first generates a wavefield dominated by downward propagation, then generates a 'first' upward propagating wavefield, then a 'second' downward propagating field, etc. In this manner, multiple reflections (class one multiples) are accounted for in a controlled manner. The Bremmer series in acoustic media have already found application in Van Stralen *et al.* (1998) where the one-way wave operator is approximated with an accurate optimal finite-difference algorithm based on a rational expansion as opposed to a GS expansion.

The propagator that generates the Bremmer series can be represented by a Hamiltonian path integral (De Witte-Morette *et al.*, 1979; Fishman & McCoy, 1984a; Fishman & McCoy, 1984b; De Hoop, 1996) that accounts for not only the energy traveling along the ray but also for the transport along non-stationary paths. These path integrals contain all possible multi-pathing. In the path integral, 'time' is identified with depth, and 'momenta' are identified with the horizontal wave slownesses which, in the ray-theoretic limit, coincide with the horizontal components of the gradient of travel time. The (square-root) Hamiltonian, appearing in the phase of the path integral, is identified with vertical wave slowness, which, in the ray-theoretic limit, coincides with the vertical component of the gradient of travel time (De Hoop, 1996).

The problem with the path integrals is the computational complexity of their numerical evaluation. De Hoop *et al.* (1999) have developed a method that dramatically reduces the computational complexity of such evaluation, at the cost of approximating the acoustics (the shape of wavefronts). The result is an algorithm that, for each propagation step, is built from the

sequence: forward Fourier transform, multiplication, inverse Fourier transform, multiplication -where the transform is in the horizontal directions and may be windowed. We have designed a hierarchy of increasingly accurate approximations. Underlying these approximations is an expansion of the medium wave-speed model simultaneously into magnitude and smoothness of variation.

The original phase-screen method was designed for multiple downward scattering of waves, the downward direction being the preferred direction of propagation. It included phenomena such as focusing and defocusing associated with multi-pathing. The applicability of the phase-screen method generally requires that the screen interval satisfies the following criteria: small medium variations (weak scattering), transversely smooth medium variations (narrow-angle scattering), and even smoother variations in the preferred direction (negligible backscattering). With the GS approach, we access the accuracy of the phase-screen method, and generalize it to larger-contrast, wider-angle, and back-scattering.

The concept of screen approximations to the propagation of waves has been around for many years. The phase-screen approximation has been applied to light transmission through the atmosphere (Ratcliffe, 1956; Mercier, 1962; Filice, 1984; Martin & Flatté, 1988), propagation of light in optical fibers (Feit & Fleck, 1978), propagation of radio signals through the ionosphere (Buckley, 1975; Bramley, 1977; Knepp, 1983), propagation of acoustic waves in the ocean (Flatté *et al.*, 1979; Thomson & Chapman, 1983), and propagation of seismic waves in the earth (Stoffa *et al.*, 1990). More recently, the phase-screen method has been extended to elastic waves (Fisk & McCartor, 1991; Fisk *et al.*, 1992; Wu, 1994).

We analyze the accuracy of the GS method in complex structures using synthetic models that exhibit significant multi-pathing: the IFP 2D Marmousi model and the SEG-EAGE 3D salt model. These two models represent two fundamentally different geological situations. In the Marmousi model, complexity arises from faulting and tectonic deformation in a sedimentary region. In the SEG-EAGE 3D salt model, it arises from the intrusion of a salt body the

wave speed of which is significantly higher than in the surrounding formations. These models commonly yield poor imaging below these complex structures. With the help of the GS propagator, which we prove to be accurate in these situations, we shall illustrate that the origin of this problem is possibly associated with multi-pathing.

We first present the GS representation of the thin-slab propagator as well as the reflection operator. These results are then cast into numerical algorithms, and our accuracy analysis is carried out by modeling primarily. We analyze the migration operator before stacking that is conventionally performed in the process of imaging. We focus on multi-pathing and ‘second’-arrival energy. We illustrate the modeling capacity of the GS method in 2D and 3D. For completeness, we show some prestack depth migration results in 2D.

Throughout this paper, we assume that the medium is isotropic. In a companion paper (Le Rousseau & De Hoop, 1999), we extend the method to media that are transversely isotropic with vertical symmetry axis.

THE SCALAR GENERALIZED-SCREEN PROPAGATOR

The scalar one-way Green’s function

Selecting the direction of preference along the x_3 -axis (or ‘vertical’ axis) and denoting the remaining (‘transverse’ or ‘horizontal’) coordinates by x_μ , $\mu = 1, 2$, the one-way acoustic Green’s function $\mathcal{G}^{(\pm)}$ is defined by an equation of the form

$$[\partial_3 \mp i\omega\Gamma(x_\mu, x_3; D_\nu)] \mathcal{G}^{(\pm)}(x_\mu, x_3; x'_\nu, x'_3) = \delta(x_\mu - x'_\mu) \delta(x_3 - x'_3) \quad (1)$$

in the frequency-space domain. The left-hand side of equation (1), $\partial_3 \mp i\omega\Gamma$, is the one-way wave operator. The choice of sign discriminates upgoing ($\mathcal{G}^{(-)}$) from downgoing ($\mathcal{G}^{(+)}$) Green’s functions. For uniform density ρ , the operator Γ satisfies the characteristic equation,

$$\Gamma^2 = A, \quad A = c^{-2} - D_\nu D_\nu, \quad (2)$$

where c is the medium wave speed and

$$D_\nu \equiv \frac{1}{i\omega} \partial_\nu , \quad (3)$$

has the interpretation of *horizontal slowness* operator; $\Gamma = \Gamma(x_\mu, x_3; D_\nu)$ is the *vertical slowness* operator. In equation (2) and throughout the paper we use the summation convention for repeated indices.

For variable density media, De Hoop (1996) derived that

$$\Gamma^2 = -D_\nu D_\nu + \kappa\rho - \rho^{-1}(D_\nu\rho) D_\nu - \rho^{-1}(D_\nu D_\nu\rho) + \rho^{-2}(D_\nu\rho)(D_\nu\rho) , \quad (4)$$

equal to the transverse Helmholtz operator in the acoustic pressure-normalization analog (De Hoop, 1996; De Hoop *et al.*, 1999); ρ is the volume density of mass [kg/m³], and κ is the compressibility [Pa⁻¹], with the wave speed defined as $c^{-2} = \kappa\rho$.

The thin-slab propagator.—In the present development, it is advantageous to use the Laplace transform with respect to time, t , and the Fourier transform with respect to the horizontal spatial coordinates, x_μ . We introduce the notation

$$s = -i\omega , \quad (5)$$

$$\alpha_\nu = \frac{1}{i\omega} k_\nu = -\frac{1}{s} k_\nu , \quad (6)$$

where ω and k_ν are the frequency and the horizontal wavenumber components. In the Laplace (s) domain with $\text{Re}(s) > 0$, the operator A becomes strictly elliptic, which enables us to consider any of its fractional powers with the aid of pseudodifferential calculus (Treves, 1980). Here, we are interested in its square root, Γ . Using the Fourier transform with respect to the horizontal spatial coordinates we can associate with Γ and A their ‘left symbols’ (Hörmander, 1985; Treves, 1980), γ and a respectively, i.e., let ϕ be a test function, then

$$(\Gamma\phi)(x_\mu, x_3) = \int (s/2\pi)^2 d\alpha_1 d\alpha_2 \int dx'_1 dx'_2 \gamma(x_\mu, x_3; \alpha_\nu) \exp[-is(x_\sigma - x'_\sigma)\alpha_\sigma] \phi(x'_\nu, x_3) ,$$

$$(A\phi)(x_\mu, x_3) = \int (s/2\pi)^2 d\alpha_1 d\alpha_2 \int dx'_1 dx'_2 a(x_\mu, x_3; \alpha_\nu) \exp[-is(x_\sigma - x'_\sigma)\alpha_\sigma] \phi(x'_\nu, x_3) ,$$

where the symbol a is obtained, after equation (4), as

$$a = \alpha_\nu \alpha_\nu + \kappa \rho - \rho^{-1} (D_\nu \rho) i \alpha_\nu - \rho^{-1} (D_\nu D_\nu \rho) + \rho^{-2} (D_\nu \rho) (D_\nu \rho) ,$$

since $i \alpha_\nu$ is the left symbol of D_ν^1 . For uniform density, a reduces to $\alpha_\nu \alpha_\nu + \kappa \rho$, consistent with equation (2). Equation (2) transforms into a characteristic equation for left symbols:

$$\exp \left[-i \partial_{\alpha'_\sigma} D_{x'_\sigma} \right] \gamma(x_\mu; \alpha'_\sigma) \gamma(x'_\sigma; \alpha_\nu) \Big|_{(x'_\mu, \alpha'_\nu) = (x_\mu, \alpha_\nu)} = a(x_\mu; \alpha_\nu) , \quad (7)$$

as given by symbol calculus of pseudodifferential operators (Treves, 1980; De Hoop, 1996, equation (A12)).

With the vertical slowness left symbol, the one-way Green's function, $\mathcal{G}^{(\pm)}$, from equation (1) can be represented by a Hamiltonian path-integral representation (De Hoop *et al.*, 1999; Fishman & McCoy, 1984b; Schulman, 1981; Cohen-Tannoudji *et al.*, 1977). We define the scalar one-way propagator, $g^{(\pm)}$, through

$$\mathcal{G}^{(\pm)} = \pm H(\pm[x_3 - x'_3]) g^{(\pm)} ,$$

where the Heaviside function H generates the Dirac distribution in equation (1) (cf. Appendix A). For a sufficiently small vertical step Δx_3 (thin slab), and a medium sufficiently smooth, the Hamiltonian path-integral representation for the one-way thin-slab propagator reduces to (De Hoop *et al.*, 1999):

$$\begin{aligned} g^{(\pm)}(x_\mu, x_3; x'_\nu, x'_3) &\simeq \\ &\int (1/2\pi)^2 dk_1 dk_2 \exp[i k_\sigma (x_\sigma - x'_\sigma)] \exp[\pm i \omega \gamma(x_\mu, \bar{x}_3; i k_\nu / \omega) \Delta x_3] \\ &= \int (s/2\pi)^2 d\alpha_1 d\alpha_2 \exp[-i s \alpha_\sigma (x_\sigma - x'_\sigma)] \exp[\mp s \gamma(x_\mu, \bar{x}_3; \alpha_\nu) \Delta x_3] , \quad (8) \end{aligned}$$

with

$$\Delta x_3 = x_3 - x'_3 ,$$

$${}^1(D_\nu \phi)(x_\mu, x_3) = \int (s/2\pi)^2 d\alpha_1 d\alpha_2 \int dx'_1 dx'_2 i \alpha_\nu \exp[-i s (x_\sigma - x'_\sigma) \alpha_\sigma] \phi(x'_\nu, x_3)$$

$$\bar{x}_3 = x_3 - \frac{1}{2}\Delta x_3 = x'_3 + \frac{1}{2}\Delta x_3 .$$

In the limit of a laterally homogeneous thin slab, γ will not depend on x_μ , and the thin-slab propagator reduces to Gazdag's phase-shift operator (Gazdag, 1978). The operator is composed of a forward Fourier transform, a multiplication by a phase factor (the phase is proportional to the vertical slowness) and an inverse Fourier transform. In the general case of equation (8), the thin-slab propagator has a similar structure except that the phase factor is dependent upon the output point, x_μ . Every output point requires its own evaluation of equation (8), which represents a considerable computational effort. The GS approximation of the thin-slab propagator enforces a simplification of this computational complexity, while allowing laterally varying media.

High-frequency approximation.—Throughout this paper, we will use a ‘high-frequency’ approximation. Then the pseudodifferential operator Γ reduces to its principal part Γ_1 , and the associated left symbol, γ , reduces to its principal symbol, γ_1 . The principal symbol, γ_1 , follows from taking the high-frequency limit of equation (7) (cf. Appendix B):

$$\gamma_1(x_\mu, x_3; \alpha_\nu) = \sqrt{[c(x_\mu, x_3)]^{-2} + \alpha_\nu \alpha_\nu} . \tag{9}$$

The triplet $(i\alpha_1, i\alpha_2, \gamma_1)$ represents the components of the gradient of the travel time. Then, the scalar one-way thin-slab propagator becomes

$$g^{(\pm)}(x_\mu, x_3; x'_\nu, x'_3) \simeq \int (s/2\pi)^2 d\alpha_1 d\alpha_2 \exp[-is \alpha_\sigma (x_\sigma - x'_\sigma)] \exp[\mp s \gamma_1(x_\mu, \bar{x}_3; \alpha_\nu) \Delta x_3] . \tag{10}$$

Generalized-screen principal-slowness surface

The contrast formulation.—For the subsequent analysis, we employ a ‘contrast formulation’ that allows us to take lateral heterogeneity into account in the thin-slab propagation.

In the slab $[x'_3, x_3]$ we introduce a background medium with wave speed c^0 . The background medium is constant in the slab, but may vary from one slab to another. We express this by letting $c^0 = c^0(x_3)$. A medium perturbation term u is then introduced as

$$u(x_\mu, x_3) = [c(x_\mu, x_3)]^{-2} - [c^0(x_3)]^{-2} . \quad (11)$$

To avoid having an artificial branch point enter the propagating-wave domain (see below), we impose the condition

$$c^0(x_3) \leq c(x_\mu, \zeta) \text{ for } \zeta \in [x'_3, x_3] . \quad (12)$$

We will expand the principal symbol of the vertical slowness left symbol, γ_1 , into the perturbation u about the background medium.

Generalized-screen expansion.—Assuming small vertical medium variation across the thin slab, i.e., if the thin slab is sufficiently small, we set

$$\begin{aligned} \gamma^0(\zeta; \alpha_\nu) &= \sqrt{[c^0(x_3)]^{-2} + \alpha_\nu \alpha_\nu} \\ &= \gamma^0(x_3; \alpha_\nu) \text{ for } \zeta \in [x'_3, x_3] , \end{aligned} \quad (13)$$

the vertical slowness associated with the background medium. The principal symbol of the vertical slowness, γ_1 , can then be decomposed into a background component, γ^0 , and a perturbation, γ_1^1 , i.e.,

$$\gamma_1(x_\mu, x_3; \alpha_\nu) = \gamma^0(x_3; \alpha_\nu) + \gamma_1^1(x_\mu, x_3; \alpha_\nu). \quad (14)$$

To find an explicit form for γ_1^1 we use relationship (9), which can be rewritten as

$$\begin{aligned} \gamma_1(x_\mu, x_3; \alpha_\nu) &= \sqrt{[c^0(x_3)]^{-2} + u(x_\mu, x_3) + \alpha_\nu \alpha_\nu} \\ &= \gamma^0(x_3; \alpha_\nu) \sqrt{1 + \frac{u(x_\mu, x_3)}{[\gamma^0(x_3; \alpha_\nu)]^2}} , \end{aligned} \quad (15)$$

and expand the result in a Taylor series according to

$$\begin{aligned} \gamma_1(x_\mu, x_3; \alpha_\nu) &= \gamma^0(x_3; \alpha_\nu) + \gamma_1^1(x_\mu, x_3; \alpha_\nu) \\ &= \gamma^0(x_3; \alpha_\nu) + \sum_{j=1}^n a_j \frac{[u(x_\mu, x_3)]^j}{[\gamma^0(x_3; \alpha_\nu)]^{2j-1}} + o(u(x_\mu, x_3))^n, \end{aligned} \quad (16)$$

where

$$a_j = (-1)^{j+1} \frac{1 \cdot 2 \cdots (2j-3)}{j! 2^j}. \quad (17)$$

In practice, we shall limit ourselves to the fourth-order expansion,

$$\begin{aligned} \gamma_1(x_\mu, x_3; \alpha_\nu) &= \gamma^0(x_3; \alpha_\nu) + \frac{1}{2} \frac{u(x_\mu, x_3)}{\gamma^0(x_3; \alpha_\nu)} - \frac{1}{8} \frac{[u(x_\mu, x_3)]^2}{[\gamma^0(x_3; \alpha_\nu)]^3} + \frac{1}{16} \frac{[u(x_\mu, x_3)]^3}{[\gamma^0(x_3; \alpha_\nu)]^5} \\ &\quad - \frac{5}{128} \frac{[u(x_\mu, x_3)]^4}{[\gamma^0(x_3; \alpha_\nu)]^7} + o(u(x_\mu, x_3))^4. \end{aligned} \quad (18)$$

It is important to note that in each term of the expansion, the dependencies on x_μ and on α_ν are factorized. This property will induce the structure of the GS propagator. Justification of expansion (16) is given in De Hoop *et al.* (1999), where the full symbol γ is analyzed; here we have restricted ourselves to its principal symbol, γ_1 . Where normal mode expansions of the one-way propagator apply, the factorization, in fact, occurs naturally (Fishman *et al.*, 1999).

Phase-screen and split-step Fourier approximations.—The phase-screen approximation follows from expansion (16) by setting $n = 1$ and approximating $1/\gamma^0$ by its zero-order Taylor expansion in α_ν about 0 (vertical propagation),

$$\gamma_1(x_\mu, x_3; \alpha_\nu) \simeq \gamma^0(x_3; \alpha_\nu) + \frac{1}{2} c^0 u(x_\mu, x_3). \quad (19)$$

This leads to the approximation of the vertical slowness symbol employed by Stoffa *et al.* (1990), since

$$u = c^{-2} - (c^0)^{-2} \simeq 2(c^0)^{-1}(c^{-1} - (c^0)^{-1}),$$

which yields with equation (19),

$$\gamma_1(x_\mu, x_3; \alpha_\nu) \simeq \gamma^0(x_3; \alpha_\nu) + [c(x_\mu, x_3)]^{-1} - [c^0(x_3)]^{-1}, \quad (20)$$

as found in the split-step Fourier method.

Figure 1 illustrates the principal slowness surfaces (γ_1 as a function of the horizontal slowness $p = \sqrt{-\alpha_\nu \alpha_\nu}$) of the GS expansions for $n = 1, 2$ and 3 as given in equation (16), and the split-step Fourier one. The split-step approximation approaches the actual slowness surface by simply vertically *shifting* the background slowness surface. Adding higher-order terms in the GS expansion, the *shape* of the slowness surface is improved and, hence, the accuracy for wider-angle propagation is increased. This observation indicates that for the extension to anisotropic media, the split-step approximation does not have the degree of freedom to shape the slowness surface appropriately (Le Rousseau & De Hoop, 1999; Thomsen, 1998); the influence of the anisotropic parameters occurs only at non vertical propagation.

The GS expansion as shown in equation (16) reveals the introduction of reciprocal powers of γ^0 and hence contains branch points at $\alpha_\nu \alpha_\nu = -[c^0]^{-2}$, as illustrated in Figure 1. The vicinity of the branch point should be treated carefully. To ensure that the branch point is out of the propagation regime within the thin-slab, we have chosen c^0 smaller than the minimum medium wave speed within the slab, as illustrated in Figure 1. Unlike the GS expansion, the split-step Fourier method does not suffer from the presence of a branch point. The choice of a background wave speed c^0 greater than the minimum wave speed in each thin-slab is therefore possible for this approximation. One may then choose, for example, the mean or the median of the medium velocities in the slab as a reference. Different choices yield different operators; It is not obvious how to find the ‘optimum’ background medium.

In the phase-screen approximation (cf. equation (19)), the Taylor expansion of $1/\gamma^0$ in $\alpha_\nu \alpha_\nu$ was truncated after the first term. The accuracy of this approximation is increased by

simply adding more terms, e.g.,

$$\gamma_1(x_\mu, x_3; \alpha_\nu) \simeq \gamma^0(x_3; \alpha_\nu) + \frac{1}{2} u(x_\mu, x_3) [c^0(x_3) - \frac{1}{2}\alpha_\nu\alpha_\nu(c^0(x_3))^3] , \quad (21)$$

yielding an angular correction in the vertical slowness. The accuracy, however, is bounded by the accuracy of the first-order GS expansion. Comparison of accuracy is illustrated in Figure 2. Approximation (21) is labeled as GSP1,2 in Figure 2.

The scalar generalized-screen propagator

With the analysis given in equation (16), we write equation (10) in the form

$$g^{(\pm)}(x_\mu, x_3; x'_\nu, x'_3) \simeq \int (s/2\pi)^2 d\alpha_1 d\alpha_2 \exp[-is \alpha_\sigma (x_\sigma - x'_\sigma)] \quad (22)$$

$$\cdot \exp[\mp s \{ \gamma^0(\bar{x}_3; \alpha_\nu) + \gamma_1^1(x_\mu, \bar{x}_3; \alpha_\nu) \} \Delta x_3] ,$$

where

$$\bar{x}_3 = x_3 - \frac{1}{2}\Delta x_3 = x'_3 + \frac{1}{2}\Delta x_3 . \quad (23)$$

Expanding the exponential, we seek an approximation of the propagator that matches the structure of the GS expansion. We therefore expand the perturbation term about vertical propagation and write

$$\gamma_1^1(x_\mu, \bar{x}_3; \alpha_\nu) = \gamma_1^1(x_\mu, \bar{x}_3; 0) + [\gamma_1^1(x_\mu, \bar{x}_3; \alpha_\nu) - \gamma_1^1(x_\mu, \bar{x}_3; 0)] ,$$

and

$$\exp[\mp s(\gamma_1^1(x_\mu, \bar{x}_3; \alpha_\nu) - \gamma_1^1(x_\mu, \bar{x}_3; 0)) \Delta x_3] \simeq \quad (24)$$

$$1 \mp s [\gamma_1^1(x_\mu, \bar{x}_3; \alpha_\nu) - \gamma_1^1(x_\mu, \bar{x}_3; 0)] \Delta x_3 .$$

Expanding the exponential separates dependencies of the propagator on x_μ and on α_ν , which allows spatial dependencies to be taken out of the Fourier integral (22). We have accomplished

that the inverse Fourier transforms with respect to α_ν *no longer* have to be evaluated for each x_μ *separately*, which is the key simplification of the GS propagator compared with the ‘exact’ thin-slab propagator. We obtain

$$g^{(\pm)}(x_\mu, x_3; x'_\nu, x'_3) \simeq g^{0(\pm)}(x_\mu, x_3; x'_\nu, x'_3) + g^{1(\pm)}(x_\mu, x_3; x'_\nu, x'_3) , \quad (25)$$

with

$$g^{0(\pm)}(x_\mu, x_3; x'_\nu, x'_3) = \exp[\mp s \gamma_1^1(x_\mu, \bar{x}_3; 0) \Delta x_3] \quad (26)$$

$$\cdot \int (s/2\pi)^2 d\alpha_1 d\alpha_2 \exp[-is \alpha_\sigma (x_\sigma - x'_\sigma)] \exp[\mp s \gamma^0(\bar{x}_3; \alpha_\nu) \Delta x_3] ,$$

and

$$g^{1(\pm)}(x_\mu, x_3; x'_\nu, x'_3) = \exp[\mp s \gamma_1^1(x_\mu, \bar{x}_3; 0) \Delta x_3] \quad (27)$$

$$\cdot \int (s/2\pi)^2 d\alpha_1 d\alpha_2 \exp[-is \alpha_\sigma (x_\sigma - x'_\sigma)] \exp[\mp s \gamma^0(\bar{x}_3; \alpha_\nu) \Delta x_3]$$

$$\cdot \Delta x_3 \left[\mp s (\gamma_1^1(x_\mu, \bar{x}_3; \alpha_\nu) - \gamma_1^1(x_\mu, \bar{x}_3; 0)) \right] .$$

Since

$$\gamma_1^1(x_\mu, \bar{x}_3; 0) \sim \sum_{j=1}^{\infty} a_j \frac{[u(x_\mu, \bar{x}_3)]^j}{[\gamma^0(\bar{x}_3; 0)]^{2j-1}} = [c(x_\mu, \bar{x}_3)]^{-1} - [c^0(x_\mu, \bar{x}_3)]^{-1} ,$$

which is a spatial correction term that may be found in the split-step Fourier method (Stoffa *et al.*, 1990), we obtain

$$g^{0(\pm)}(x_\mu, x_3; x'_\nu, x'_3) = \exp \left[\mp s \left([c(x_\mu, \bar{x}_3)]^{-1} - [c^0(\bar{x}_3)]^{-1} \right) \Delta x_3 \right] \quad (28)$$

$$\cdot \int (s/2\pi)^2 d\alpha_1 d\alpha_2 \exp[-is \alpha_\sigma (x_\sigma - x'_\sigma)] \exp[\mp s \gamma^0(\bar{x}_3; \alpha_\nu) \Delta x_3] .$$

The first constituent term of the GS propagator, $g^{0(\pm)}$, is the propagator of the split-step Fourier method, i.e., a propagator associated with the background medium for the thin-slab and a

correction term in space that is accurate for the vertical propagation only. The second term in the GS propagator follows as then

$$\begin{aligned}
 g^{1(\pm)}(x_\mu, x_3; x'_\nu, x'_3) &= \exp \left[\mp s \left([c(x_\mu, \bar{x}_3)]^{-1} - [c^0(\bar{x}_3)]^{-1} \right) \Delta x_3 \right] \\
 &\cdot \int (s/2\pi)^2 d\alpha_1 d\alpha_2 \exp[-is \alpha_\sigma (x_\sigma - x'_\sigma)] \exp[\mp s \gamma^0(\bar{x}_3; \alpha_\nu) \Delta x_3] \\
 &\cdot \Delta x_3 \left[\mp s (\gamma_1^1(x_\mu, \bar{x}_3; \alpha_\nu) - \gamma_1^1(x_\mu, \bar{x}_3; 0)) \right],
 \end{aligned} \tag{29}$$

which, upon replacing γ_1^1 by its truncated expression as in equation (16), gives

$$\begin{aligned}
 g^{1(\pm)}(x_\mu, x_3; x'_\nu, x'_3) &= \exp \left[\mp s \left([c(x_\mu, \bar{x}_3)]^{-1} - [c^0(\bar{x}_3)]^{-1} \right) \Delta x_3 \right] \\
 &\cdot \mp s \Delta x_3 \sum_{j=1}^n \left\{ a_j [u(x_\mu, \bar{x}_3)]^j \int (s/2\pi)^2 d\alpha_1 d\alpha_2 \exp[-is \alpha_\sigma (x_\sigma - x'_\sigma)] \right. \\
 &\quad \left. \cdot \exp[\mp s \gamma^0(\bar{x}_3; \alpha_\nu) \Delta x_3] \left[\frac{1}{[\gamma^0(\bar{x}_3; \alpha_\nu)]^{2j-1}} - \frac{1}{[\gamma^0(\bar{x}_3; 0)]^{2j-1}} \right] \right\}.
 \end{aligned} \tag{30}$$

The second constituent term of the GS propagator, $g^{1(\pm)}$, arises from the higher-order terms of the GS expansion. We call n the order of the GS approximation. As mentioned, the higher the order, the higher the accuracy for wide-angle propagation.

The split-step Fourier propagator simply yields a shuttling between the frequency-horizontal space and frequency-horizontal slowness domains and a multiplication in each domain. Each additional term of the GS expansion (16) requires an additional inverse Fourier transform in space as expressed in equation (30). As the *computational complexity* of the downward continuation in the split-step Fourier method is proportional to $2N_1 N_2 \log_2 N_1 N_2$ (N_μ denoting the numbers of samples in the x_μ -direction), the complexity of our n^{th} -order GS approach is proportional to $(2 + n)N_1 N_2 \log_2 N_1 N_2$.

Normalization of the scalar generalized-screen propagator

The Taylor expansion of the exponential in equation (24) destroys the unitarity of propagator (8) and hence the amplitude characteristics of the propagator; depending on the wavenum-

ber, or the local angle of propagation, part of the energy may be amplified or attenuated incorrectly. It can also lead to a numerical algorithm that is unstable over a large range of downward continuation. To restore, approximately, the amplitude behavior, we apply a normalizing operator and obtain the GS propagator g_{GSP}

$$g_{GSP}^{(\pm)}(x_\mu, x_3; x'_v, x'_3) = g^{0(\pm)}(x_\mu, x_3; x'_v, x'_3) \mathcal{N} \left[1 + \frac{g^{1(\pm)}(x_\mu, x_3; x'_v, x'_3)}{g^{0(\pm)}(x_\mu, x_3; x'_v, x'_3)} \right],$$

the division being carried out in some stable sense, and the normalizing operator \mathcal{N} being given by

$$\mathcal{N}[1 + p + iq] = \exp(iq) \left| 1 + \frac{p}{1 + iq} \right|^{-1} \left[1 + \frac{p}{1 + iq} \right].$$

In effect, this normalization corrects for the error introduced by the expansion of the exponential in equation (24), and restores the amplitude behavior exactly in the case of a constant perturbation u , i.e., a medium with wave speed higher than the reference wave speed.

THE SCALAR GENERALIZED-SCREEN ALGORITHM

Here, we discuss the GS algorithm based upon equations (22) through (30). We denote the (one-way) wavefield by W , and carry out the wave propagation in the frequency domain, with each frequency component computed independently. The downward continuation for modeling and imaging with the one-way propagator is performed according to the decomposition of the vertical slowness symbol into one background term and a series of perturbation terms as in equation (16).

Let the current depth be set to $x'_3 = z$, and set $\bar{x}_3 = x'_3 + \frac{1}{2}\Delta x_3$ as before. Following equation (30), we introduce the intermediate field quantities w_0, \dots, w_n according to (*step 1*)

$$w_0(x_\mu, s) = \exp \left[-s \Delta x_3 \left([c(x_\mu, \bar{x}_3)]^{-1} - [c^0(\bar{x}_3)]^{-1} \right) \right] W(x_\mu, x'_3, s),$$

$$w_1(x_\mu, s) = -s \Delta x_3 a_1 u(x_\mu, \bar{x}_3) w_0(x_\mu, s),$$

$$\begin{aligned}
 w_2(x_\mu, s) &= -s \Delta x_3 a_2 u^2(x_\mu, \bar{x}_3) w_0(x_\mu, s), \\
 &\vdots \\
 w_n(x_\mu, s) &= -s \Delta x_3 a_n u^n(x_\mu, \bar{x}_3) w_0(x_\mu, s).
 \end{aligned}$$

w_0 represents the split-step Fourier term; the higher-order terms increase the accuracy for wider-angle propagation. The intermediate field quantities are then Fourier transformed to the horizontal-wavenumber domain (*step 2*),

$$\begin{aligned}
 \tilde{w}_j(\alpha_\nu, s) &= \int w_j(x_\mu, s) \exp[-i x_\sigma k_\sigma] dx_\mu \\
 &= \int w_j(x_\mu, s) \exp[is x_\sigma \alpha_\sigma] dx_\mu, \quad j = 0, \dots, n.
 \end{aligned} \tag{31}$$

The wavefield at depth $x_3 = z + \Delta x_3$ then follows as

$$\begin{aligned}
 \tilde{W}(x_3; \alpha_\nu, s) &= \tilde{w}_0(\alpha_\nu, s) \exp[-s \Delta x_3 \gamma^0(\bar{x}_3; \alpha_\nu)] \\
 &\cdot \mathcal{N} \left[1 + \frac{\tilde{w}_1(\alpha_\nu, s)}{\tilde{w}_0(\alpha_\nu, s)} \left(\frac{1}{\gamma^0(\bar{x}_3; \alpha_\nu)} - c^0(\bar{x}_3) \right) \right. \\
 &\quad \left. + \dots + \frac{\tilde{w}_n(\alpha_\nu, s)}{\tilde{w}_0(\alpha_\nu, s)} \left(\frac{1}{[\gamma^0(\bar{x}_3; \alpha_\nu)]^{2n-1}} - [c^0(\bar{x}_3)]^{2n-1} \right) \right].
 \end{aligned}$$

(*step 3*). Finally, we carry out the inverse Fourier transform $\tilde{W}(x_3; \alpha_\nu, s) \rightarrow W(x_\mu, x_3; s)$, (*step 4*).

The sequence of steps illustrates the shuttling between the frequency-horizontal space domain and frequency-horizontal wavenumber domain that is performed with the GS approach. The method departs from the exact solution through the (approximate) expansion of the vertical slowness operator.

The case of a constant medium perturbation provides insight in how wavefronts evolve based on Huygens' principle (Huygens, 1690). Let the background medium be characterized by a wave speed c^0 that is 2/3 of the true wave speed. The top of Figure 3 shows (instantaneous)

wavefronts constructed as the polar reciprocal of the local slowness surface shown in Figure 2. In the bottom part of Figure 3 we show numerical impulse responses of the one-way propagator for different orders of generalized screens, as well as for the split-step Fourier method. For a constant perturbation, the predicted wavefronts and the actual computed wavefronts can be overlain exactly. The exact response is plotted dashed in the top part of the figure. Note that the accuracy varies with propagation angle (or migration dip upon imaging), and that this accuracy varies with (local) medium perturbation. In all the approximations, independent of order n , the propagation speed in the horizontal directions approaches c^0 , which causes any approximate wavefront to fold inwards away from the true wavefront. Indeed, the normal to any slowness surface in Figure 2 is horizontal or converges to horizontal when the horizontal slowness is $1/c^0$. As such, the GS approximation differs, for example, from the paraxial approximation where the accuracy with dip is independent of the medium (De Hoop & De Hoop, 1992). The GS inaccuracy at horizontal propagation is inherited from the GS expansion of the vertical slowness symbol. Note, however, that for non-horizontal propagation, including very large angle propagation, any accuracy can be obtained depending on the order of the GS approximation chosen. We should also note that the large error seen here for horizontal propagation is due to the choice of c^0 : c^0 is only $2/3$ of the actual wave speed c .

Figure 4 compares 3D computations for the first four orders of the GS propagators and for the split-step Fourier method. Again, the dashed curves show the true wavefront location. From Figure 4 we conjecture that, as a rule of thumb, the split-step Fourier method is accurate up to 17° , the first-order GS is accurate up to 34° , the second-order GS up to 48° , the third-order GS up to 55° , and the fourth-order GS up to 62° , when such a perturbation occurs (the background wave speed being only $2/3$ of the actual wave speed). The rate of convergence with order is also suggestive in Figure 4. As in any Taylor expansion, the first terms in the GS expansion bring the main contribution to the operator, and the higher-order terms have lesser contributions, slowly increasing the accuracy.

THE GENERALIZED-SCREEN REPRESENTATION OF THE REFLECTION OPERATOR

The thin-slab propagator given in equation (8) is the one associated with the one-way wave equation. To recover the two-way wave propagation one has to make use of the Bremmer series, as described by De Hoop (1996). The first term of the series is the one-way wavefield; the second term is the first (class two) multiple; the third term is the second multiple, etc. The evaluation of each term of the Bremmer series requires the use of the reflection operator given as

$$R = \frac{1}{2}\Gamma^{-1}(\partial_3\Gamma) , \tag{32}$$

for constant density and a continuous medium. We associate to R its left symbol, r ,

$$R\phi(x_\mu, x_3) = \int (s/2\pi)^2 d\alpha_1 d\alpha_2 \int dx'_1 dx'_2 r(x_\mu, x_3; \alpha_\nu) \exp[-is(x_\sigma - x'_\sigma)\alpha_\sigma] \phi(x'_\nu, x_3) .$$

In the framework of the present ‘high-frequency’ approximation, R reduces to its principal part R_1 , with r reducing to its principal symbol r_1 .

In a similar fashion as in Appendix B, one can show that such reduction to principal symbol, yields

$$r_1 = \frac{\partial_3\gamma_1}{2\gamma_1} . \tag{33}$$

At a horizontal interface, the reflection symbol is simply the reflection coefficient, but this is not true for a non-horizontal interface. For a non-horizontal interface, the reflection of an incoming wave is split between the one-way propagation operator and the reflection operator. The reflection operator is responsible for the interaction between the up- and downgoing constituents of the wavefield. The one-way wave operator describes the transverse scattering.

Like γ_1 , the reflection symbol r_1 can be expanded by introducing the same background medium and perturbation as within the thin slab through which propagation takes place. Here,

we present the GS expansion of the reflection symbol in a medium sampled at discrete points.

At an interface located at x_3 , the reflection symbol can be expressed as

$$r_1(x_\mu, x_3; \alpha_\nu) = \frac{\gamma_1(x_\mu, x_3^+; \alpha_\nu) - \gamma_1(x_\mu, x_3^-; \alpha_\nu)}{\gamma_1(x_\mu, x_3^+; \alpha_\nu) + \gamma_1(x_\mu, x_3^-; \alpha_\nu)}, \quad (34)$$

where

$$x_3^- = x_3 - \frac{1}{2}\Delta x_3,$$

and

$$x_3^+ = x_3 + \frac{1}{2}\Delta x_3.$$

Upon introducing a background medium and a perturbation on both sides of the interface, i.e.

$$u(x_\mu, x_3^-) = [c(x_\mu, x_3^-)]^{-2} - [c^0(x_3^-)]^{-2},$$

and

$$u(x_\mu, x_3^+) = [c(x_\mu, x_3^+)]^{-2} - [c^0(x_3^+)]^{-2},$$

one can expand the reflection principal symbol with respect to these two perturbations. In the GS expansion of the one-way thin-slab propagator, the expansion of the exponential in equation (24) yields accuracy in the vicinity of vertical propagation. We want to enforce such accuracy for the expansion of the reflection operator as well, and thus write

$$r_1(x_\mu, x_3; \alpha_\nu) = r_1(x_\mu, x_3; 0) + [r_1(x_\mu, x_3; \alpha_\nu) - r_1(x_\mu, x_3; 0)]. \quad (35)$$

We then expand $r_1(x_\mu, x_3; \alpha_\nu) - r_1(x_\mu, x_3; 0)$ with respect to the perturbations u at x_3^- and x_3^+ , which, to first order, yields

$$r_1(x_\mu, x_3; \alpha_\nu) \simeq r_1(x_\mu, x_3; 0) + a_1^-(x_3; \alpha_\nu)u(x_\mu, x_3^-) + a_1^+(x_3; \alpha_\nu)u(x_\mu, x_3^+), \quad (36)$$

with

$$a_1^-(x_3; \alpha_\nu) = \frac{-\frac{\gamma^0(x_3^+, \alpha_\nu)}{\gamma^0(x_3^-, \alpha_\nu)} \left([c^0(x_3^+)]^2 + [c^0(x_3^-)]^2 \right) + c^0(x_3^-) c^0(x_3^+) + \frac{[c^0(x_3^-)]^3}{c^0(x_3^+)}}{\sigma(x_3^+, x_3^-, \alpha_\nu)} + \frac{2\alpha_\nu \alpha_\nu [c^0(x_3^-)]^3 c^0(x_3^+) \left(1 + \frac{\gamma^0(x_3^+, \alpha_\nu)}{\gamma^0(x_3^-, \alpha_\nu)} \right)}{\sigma(x_3^+, x_3^-, \alpha_\nu)}, \quad (37)$$

and

$$a_1^+(x_3; \alpha_\nu) = \frac{\frac{\gamma^0(x_3^-, \alpha_\nu)}{\gamma^0(x_3^+, \alpha_\nu)} \left([c^0(x_3^+)]^2 + [c^0(x_3^-)]^2 \right) - c^0(x_3^-) c^0(x_3^+) - \frac{[c^0(x_3^+)]^3}{c^0(x_3^-)}}{\sigma(x_3^+, x_3^-, \alpha_\nu)} - \frac{2\alpha_\nu \alpha_\nu [c^0(x_3^+)]^3 c^0(x_3^-) \left(1 + \frac{\gamma^0(x_3^-, \alpha_\nu)}{\gamma^0(x_3^+, \alpha_\nu)} \right)}{\sigma(x_3^+, x_3^-, \alpha_\nu)}, \quad (38)$$

where

$$\sigma(x_3^+, x_3^-, \alpha_\nu) = \left[\gamma^0(x_3^+, \alpha_\nu) + \gamma^0(x_3^-, \alpha_\nu) \right]^2 \left[c^0(x_3^+) + c^0(x_3^-) \right]^2.$$

The superscript ‘-’ refers to the upper medium and the superscript ‘+’ to the lower one, whereas the subscript refers to the order in the GS expansion. We have

$$a_1^-(x_3; 0) = 0, \quad a_1^+(x_3; 0) = 0.$$

Figure 5 illustrates the GS expansion of the reflection symbol at an interface where the upper medium is characterized by a constant perturbation and the lower medium by a zero perturbation. In the top of the figure, the exact reflection symbol (dashed) and the first two GS approximations are shown as a function of the horizontal slowness $p = \sqrt{-\alpha_\nu \alpha_\nu}$. The bottom part of Figure 5 shows the relative error of the first two GS approximations. Note the increasing angular accuracy as the order of the GS expansion increases. This accuracy will be required to predict multiple scattering at large offset.

Note that to compute the n^{th} term in the Bremmer series, the reflection operator is only applied n times to the wavefield while a cascade of thin-slab GS propagators is applied for

each of the terms. Such cascade implies an accumulation of errors associated with the inaccuracies of the thin-slab GS propagator (e.g. propagation very close to the horizontal direction). Such accumulation of error does not occur when applying the GS reflection operator, since we usually consider the first few terms in the Bremmer series only.

The GS representation (here, first order) of the principal part of the reflection operator then follows as

$$(R_1\phi)(x_\mu, x_3) \simeq \int (s/2\pi)^2 d\alpha_1 d\alpha_2 \int dx'_1 dx'_2 \exp[-is(x_\sigma - x'_\sigma)\alpha_\sigma] \quad (39)$$

$$\cdot \left[r_1(x_\mu, x_3; 0) + a_1^-(x_3; \alpha_\nu)u(x_\mu, x_3^-) + a_1^+(x_3; \alpha_\nu)u(x_\mu, x_3^+) \right] \phi(x'_\nu, x_3) ,$$

which can be written as

$$(R_1\phi)(x_\mu, x_3) \simeq r_1(x_\mu, x_3; 0)f(x_\mu, x_3) \quad (40)$$

$$+ u(x_\mu, x_3^-) \int (s/2\pi)^2 d\alpha_1 d\alpha_2 \int dx'_1 dx'_2 a_1^-(x_3; \alpha_\nu) \exp[-is(x_\sigma - x'_\sigma)\alpha_\sigma] \phi(x'_\nu, x_3)$$

$$+ u(x_\mu, x_3^+) \int (s/2\pi)^2 d\alpha_1 d\alpha_2 \int dx'_1 dx'_2 a_1^+(x_3; \alpha_\nu) \exp[-is(x_\sigma - x'_\sigma)\alpha_\sigma] \phi(x'_\nu, x_3) ,$$

yielding the reflection operator (Schwartz) kernel \mathcal{R}_1 (De Hoop *et al.*, 1999; Schwartz, 1966; Treves, 1967)

$$\mathcal{R}_1(x_\mu, x'_\nu, x_3) \simeq r_1(x_\mu, x_3; 0) \delta(x_\mu - x'_\mu) \quad (41)$$

$$+ u(x_\mu, x_3^-) \int (s/2\pi)^2 d\alpha_1 d\alpha_2 \int dx'_1 dx'_2 a_1^-(x_3; \alpha_\nu) \exp[-is(x_\sigma - x'_\sigma)\alpha_\sigma]$$

$$+ u(x_\mu, x_3^+) \int (s/2\pi)^2 d\alpha_1 d\alpha_2 \int dx'_1 dx'_2 a_1^+(x_3; \alpha_\nu) \exp[-is(x_\sigma - x'_\sigma)\alpha_\sigma] .$$

Equations (40) and (41) can directly be cast into a numerical algorithm. Each additional term in the GS expansion of the reflection operator requires two additional Fourier transforms.

BRANCH POINTS

The terms in GS expansion contain powers of $1/\gamma^0$ increasing with order [cf. equation (16)]. These powers induce branch points at $\alpha_\nu \alpha_\nu = -[c^0]^{-2}$, corresponding to grazing propagation in the background medium (cf. Figure 1). The branch points also appear in expansion (30) for the GS propagator.

For a constant-perturbation medium, the normalization operator exactly compensates the errors arising from the expansion of the exponential in equation (24). Yet, in laterally heterogeneous media such as the Marmousi model (cf. Figure 6), these approximations can create errors that can be boosted by large values of $1/\gamma^0$ close to the branch point. Figure 7 shows a snapshot of the wave field, computed with the second-order GS algorithm, in the region of the Marmousi model shown in Figure 6 when the wavenumber is allowed to get close to the branch point. The source is located at a star in Figure 6. The result is noisy; the noise is associated with high-angle propagation, i.e., when wavenumbers reach the vicinity of the branch point.

In equation (30), the path of integration in the α_1 -plane should be chosen appropriately around the branch cuts. To avoid getting too close to the artificial branch points, we use contour deformation in the complex plane, as illustrated in Figure 8. Comparing the result in Figure 7 with that in Figure 9, where the contour deformation has been applied, note the removal of the noise associated with high-angle propagating energy.

In practice, we apply the contour deformation to all factors appearing in the GS algorithm (the values of γ^0 are computed along such a path) except for the intermediate field quantities in the wavenumber domain. These are assumed to vary smoothly away from the real axis and hence are approximated by their values on the real axis as given by the Fourier transforms. We therefore make a zero-order Taylor approximation for the regions where the contour departs from the real axis. The higher the power of $[\gamma^0]^{-1}$, the further the path should depart from the real axis in the vicinity of the branch points; thus we use different deformations for the

different terms in the GS expansions.

ACCURACY ANALYSIS

We illustrate the accuracy of the GS algorithm for two scenarios: the 2D Marmousi model, and the SEG-EAGE 3D salt model. Our analysis emphasizes numerical modeling. We generate Green's functions and focus our observations on second-arrival energy and multi-pathing. Imaging invokes an averaging (stacking) process; to learn about the prestack migration operator, we hence favor to analyze modeling instead. We shall, however, show depth-migration results in the Marmousi model.

Modeling

Marmousi model.—The medium complexity and the maximum propagation angle determine the sophistication of the approximation required. To illustrate this, we consider a region of the Institut Français du Pétrole (IFP)'s Marmousi model that includes the target reservoir (Figure 6). A point source (star) is located at the reservoir horizon, below a complex part of the model (anticline, unconformity, faults) that has significant horizontal wave speed variations. Being based on actual geology (Bourgeois *et al.*, 1991), the Marmousi model introduces complexities that can be encountered in practice. The source is excited at time $t = 0$, and the field is imaged at time $t = 0.95$ s, creating the snapshots in Figure 10 through Figure 13. For comparison, we modeled the two-way wavefield with the full acoustic wave equation (finite-difference time-domain, second order in space, second order in time), and shall use that wavefield (Figure 10) as a reference (the computational complexity of the full acoustic wave equation method in 2D, and even more so in 3D, compares unfavorably with the fast algorithms developed in this paper). In modeling the upgoing wavefield, we compare the GS method with the split-step Fourier and the phase-shift-plus-interpolation (PSPI) methods. In the PSPI method (Gazdag & Sguazzero, 1984), wave components are upward or downward continued as if the medium were laterally homogeneous but using several reference velocities to accommodate lateral wave

speed variations: in the frequency-space domain, at any point in depth, an interpolation is performed using two fields associated with the two adjacent reference velocities.

Unlike the GS methods, the split-step Fourier method does not suffer from the presence of a branch point. We can therefore use a background wave speed c^0 that is greater than the minimum wave speed in each thin-slab. We use the arithmetic mean of the wave speed across the thin-slab as a reference wave speed. Use of the median ($\frac{1}{2}(v_{max} - v_{min})$) for the reference wave speed gives a poor result (not shown here). Use of the same reference wave speed as for the GS method (i.e., the minimum wave speed in the thin slab) yields even poorer result, for it increases the contrast between the true medium and the background medium.

With the number of reference velocities chosen for the PSPI method, we guaranteed a better accuracy, but at higher cost, than that of the split-step Fourier method. To compare algorithm accuracies, we look at the degree at which the wavefront is curved downward or upward with respect to the full-acoustic wave-equation generated wavefront. The split-step Fourier (Figure 11) result gives an impulse response with a wider shape (upward curved) for the first arrival than the full-wave result, whereas the PSPI method (Figure 12) gives a correct general shape for the first arrival. Neither of these methods gives, however, accurate images of the second-arrival energy (although the PSPI method still yields a better result). This second-arrival energy results from multi-pathing associated with the complexity and the heterogeneity of the Marmousi model. The multi-pathing here occurs with scattering at reasonably wide angles. For the split-step Fourier method, the limited accuracy for wide-angle propagation explains the poor modeling for the second-arrival energy. For the PSPI method, inaccuracies are attributable to the *linear* interpolation scheme.

To begin with the results of the various orders of the GS method, the second-order algorithm (Figure 9) creates a wave front whose shape, as expected, is slightly curved downward with respect to the full-acoustic wave-equation wavefront. As the order of the GS expansion increases, the GS wavefront matches the true one more closely. The wavefront of the fourth-

order solution (Figure 13) closely approaches the true wavefront. With the second-order GS method (Figure 9) one can already see good definition of the second-arrival energy, due to a higher accuracy for wide-angle propagation than that in the split-step Fourier method. The better positioning and modeling of the later-arrival energy constitutes a key contribution to the imaging of complex structures such as those in the Marmousi model where these arrivals carry a significant part of the energy. Observe that subtle differences in Figures 11 through 13 represent differences in positioning of the order of a hundred meter according to the scale used.

Furthermore, when taking multiples into account, wide-angle propagation can be particularly significant, as mentioned before. Incorporating multiples is achieved with the use of the Bremmer series (De Hoop, 1996; Van Stralen *et al.*, 1998; De Hoop *et al.*, 1999). It is illustrated in Figure 14, where the fourth-order GS algorithm is used to calculate the first three terms of the Bremmer series. The first term corresponds to the upcoming energy as given by the one-way operator. The second term corresponds to energy that first travels upward then downward. The third term corresponds to energy that travels upward, downward and upward again. Here, we also make use of the first-order GS representation of the reflection operator as described before. Note that some of the multiple events found in Figure 10 are missing because they would belong to yet higher-order terms in the Bremmer series. Note in Figure 14 that some branches of the wavefronts do propagate almost horizontally and accurate results require higher order GS.

SEG-EAGE 3D salt model.—For a 3D modeling demonstration, we use the SEG-EAGE 3D salt model. Significant multi-pathing occurs in this model, and we shall illustrate how well the GS propagator accounts for this. Figure 15 shows two vertical profiles of wave speed across the SEG-EAGE 3D salt model, one parallel to the so-called in-line direction, and the second one parallel to the orthogonal cross-line direction. The profiles intersect at the center of the model. As in the Marmousi model, we place a point source in the zone of interest, i.e. beneath

the salt body. The source location is represented by an asterisk in Figure 15. Note the staircase shape of the base of the salt body. We expect this artificial roughness, which is due to the coarse sampling of the model in depth, to create diffractions that will appear as ‘noise’ in the wavefield.

In our example, the source is excited at time $t = 0$ and we use the second-order GS algorithm to image the field at time $t = 1.2$ s (snapshots in Figure 16 through Figure 20). Both the in-line section in Figure 16 and the cross-line section in Figure 17 show that second arrivals carry a significant part of the upgoing energy. They both show that, with the geometry of the salt body, partial waveguiding can occur, which could imply that a significant part of information is contained at large offsets in the scattered field recorded at the surface. Note the occurrence of a triplication in the cross-line section in Figure 17. The various horizontal sections of the 3D image (Figure 18 through Figure 20) illustrate the strong imprint that the salt structure imposes on the wavefront. The deepest slices (Figure 18) intersect the salt body, which explains the higher ‘noise’ level also visible in the vertical sections; this noise, again, corresponds to diffracted energy from the rough salt bottom.

Imaging

Laterally varying medium.—The difference in accuracy between the split-step Fourier method and the GS approach is illustrated with a 2D imaging experiment (Figure 21). The 2D section is composed of various reflectors with dips ranging from 0° to 75° . The wave speed profile is characterized by a gradient with a horizontal component of 0.1 s^{-1} and a vertical component of 0.4 s^{-1} . Figure 21 shows results after migrations of a zero-offset section (not shown) with the split-step Fourier algorithm and the fourth-order GS method. In the split-step Fourier result, reflectors steeper than about 45° are mispositioned with an error that grows with dip. Again, the accuracy with dip is a function of the lateral medium variation for both the split-step Fourier method and the GS approach. In the GS generated section, reflectors are

accurately positioned because the wide-angle propagation, associated with the steepest events, is better handled. Note that the steepest event appears weaker on the GS generated section than on the split-step Fourier section. This is due to the proximity of the branch point to the propagation angles associated with the steepest reflector dip. The cascade of the expansion of the thin-slab propagator and the normalization are progressively less accurate for the phase as one departs from vertical propagation and constant medium perturbation. This introduces some amplitude inaccuracy.

Application to prestack depth migration.—To illustrate the accuracy of the different GS expansions for imaging, we incorporated the GS algorithm in prestack depth migration of shot gathers using the entire Marmousi data set (Figure 22). In the migration procedure, the fields associated with the source and receivers are downward continued. For each point in the subsurface the two fields are correlated at zero time lag (Claerbout, 1986).

Figures 23 and 24 compare the images obtained with the split-step Fourier version of the phase-screen method and the second-order GS approach. The latter gives a better result; because of the two additional correction terms appearing in the expansion, dipping events are more accurately positioned and better focused by the GS approach. Regions where significant differences occur are highlighted in Figures 23 and 24. The anticline (above the reservoir) of the Marmousi model poses a challenge to imaging for any migration algorithm because of multi-pathing and wide-angle scattering. The GS method accommodates these phenomena better than does the split-step method and yields more continuity in, and less deformation of, the reflectors.

DISCUSSION

The generalized-screen (GS) wave extrapolation method is based on the decomposition of the medium into a background component and a perturbation. In lowest order, the GS approximation may be simplified to yield the phase-screen and split-step Fourier methods. The GS

method extends these two methods and can accommodate more significant and rapid horizontal wave speed variations. Its enhanced accuracy allows a better modeling of the wavefields in complex structures where multi-pathing is significant.

With the GS representation of the propagator is associated a vertical slowness symbol that generalizes the phase-screen and split-step Fourier symbol and has the dependencies on the spatial coordinates and the dependencies on the wavenumber factorized, inducing the structure of the GS propagator. The GS expansion of the vertical slowness symbol is justified in De Hoop *et al.* (1999). The GS expansion provides a fundamental simplification of the one-way operator; the propagator does not have to be evaluated at every output point. We obtain an algorithm that works as a shuttling between the frequency-horizontal space domain and the frequency-horizontal wavenumber domain. Each additional term in the GS expansion increases the accuracy. The additional cost is an additional Fourier transform for each additional order in the expansion. In anisotropic media such as transversely isotropic media with a vertical symmetry axis, the influence of the anisotropic parameters in the vertical slowness symbol occurs only at non-vertical propagation. The split-step-Fourier type approximation (Stoffa *et al.*, 1990) does not have the degree of freedom to account for anisotropy or to shape the slowness surface appropriately, because of its accuracy restricted to near-vertical propagation. The GS methods can be extended to these media as shown in the companion paper (Le Rousseau & De Hoop, 1999).

We illustrate the GS propagator's accuracy primarily through modeling. The mathematical accuracy analysis of the GS approximation was carried out by De Hoop *et al.* (1999). Here we focus on its numerical counterpart. We chose two synthetic models, both representative of the real world: the Marmousi model (off-shore Africa) and the SEG/EAGE 3D salt model (Gulf of Mexico). Each of these models provides insight into the capacity of the GS method to perform wave extrapolation, and shows in how it compares with the split-step Fourier method, as well as PSPI and full-wave time-domain finite-difference methods. The GS modeling capacity is

illustrated in both 2D and 3D. In the paper we focus on the computation of Green's functions rather than on imaging. Imaging invokes an averaging procedure that hides propagation inaccuracies of the various methods. For completeness, however, we show some prestack imaging results in 2D.

We have compared the GS method with the most competitive algorithms. We did not compare our results with single-pathing approach. The GS method, with its $(2+n)N_1N_2 \log_2 N_1N_2$ (n is the order of the GS approximation and N_μ are the numbers of samples in the x_μ -direction) computational complexity, makes feasible 'wave equation' modeling and imaging in 3D. Finite-difference methods extend to 3D, but yield algorithms with greater computational complexity. Nowadays, 3D surveys are common, and some areas present geologic complexities where multi-pathing cannot be ignored. Unlike traditional low-cost asymptotic methods (such as Kirchhoff) that use a unique arrival (first or maximal energy), the GS method can predict the effect of multi-pathing. In areas with geologic complexities, the GS method provides a competitive tool for imaging. The introduction of the Bremmer coupling series yields a computation of the two-way Green's functions. This creates a tool box that can be used for processing multiples, velocity analysis, and inversion (De Hoop & De Hoop, 1999). Finally, the lowest order approximations intrinsic in this paper have already found application in seismic imaging (Huang & Wu, 1996; Wu & Jin, 1997; Huang *et al.*, 1998).

ACKNOWLEDGMENTS

The authors would especially like to thank Elf Exploration Production and Mobil for financial support of this research. We also would like to thank Henri Calandra for numerous discussions. This work was also supported by the members of the Consortium Project on Seismic Inverse Methods for Complex Structures at the Center for Wave Phenomena, Colorado School of Mines.

References

- Bourgeois, A., Bourget, M., Lailly, P., Poulet, M., Ricarte, P., & Versteeg, R. 1991. Marmousi, model and data. *Proc. 1990 EAEG workshop on Practical Aspects of Seismic Data Inversion*.
- Bramley, E.N. 1977. The accuracy of computing ionospheric radiowave scintillation by the thin-phase screen approximation. *J. Atmos. Terr. Phys.*, **39**, 367–373.
- Buckley, R. 1975. Diffraction by a random phase-changing screen: a numerical experiment. *J. Atmos. Terr. Phys.*, **37**, 1431–1446.
- Claerbout, J. 1986. *Imaging the Earth's interior*. Blackwell.
- Cohen-Tannoudji, C., Diu, B., & Laloë, F. 1977. *Mécanique quantique*. Vol. 1. Hermann, Paris. Chap. 3, pages 328–335.
- De Hoop, M. V. 1996. Generalization of the Bremmer coupling series. *J. Math. Phys.*, **37**, 3246–3282.
- De Hoop, M. V., Le Rousseau, J. H., & Wu, R.-S. 1999. General formulation of screen methods for the scattering of acoustic waves. *Wave Motion*, *in print*.
- De Hoop, M.V., & Brandsberg-Dahl, S. 1999. Maslov asymptotics extension of generalized Radon transform inversion in anisotropic elastic media: a least-squares approach. *submitted to Inverse Problems*.
- De Hoop, M.V., & De Hoop, A.T. 1992. Scalar space-time waves in their spectral-domain first- and second-order Thiele approximations. *Wave Motion*, **15**, 229–265.
- De Hoop, M.V., & De Hoop, A.T. 1999. Wavefield reciprocity and optimization in remote sensing. *Proceedings of the Royal Society: Mathematical, Physical and Engineering Sciences*, *in print*.

- De Witte-Morette, C., Maheshwari, A., & Nelson, B. 1979. Path integration in non-relativistic quantum mechanics. *Physics Reports*, **50**, 255–372.
- Feit, M.D., & Fleck, J.A. 1978. Light propagation in graded-index optical fibers. *Appl. Opt.*, **17**, 3990–3998.
- Filice, J.P. 1984. *Studies of the microscale density fluctuations in the solar wind using the power law phase screen model*. Ph.D. thesis, Univ. of Calif. San Diego, La Jolla.
- Fishman, L., & McCoy, J.J. 1984a. Derivation and application of extended parabolic wave theories I. The factorized Helmholtz equation. *J. Math. Phys.*, **25**, 285–296.
- Fishman, L., & McCoy, J.J. 1984b. Derivation and application of extended parabolic wave theories II. Path integral representations. *J. Math. Phys.*, **25**, 297–308.
- Fishman, L., de Hoop, M.V., & Van Stralen, M.J.N. 1999. Exact construction of square-root Helmholtz operator symbols: The focusing quadratic profile. *submitted to J. Math. Phys.*
- Fisk, M.D., & McCartor, G.D. 1991. The phase screen method for vector elastic waves. *J. Geophys. Res.*, **96**, 5985–6010.
- Fisk, M.D., Charrette, E.E., & McCartor, G.D. 1992. A comparison of phase screen and finite difference calculations for elastic waves in random media. *J. Geophys. Res.*, **97**, 12409–12423.
- Flatté, S.M., Dashen, R., Munk, W.H., Watson, K.M., & Zachariassen, F. 1979. *Sound transmission through a fluctuating ocean*. Cambridge University Press, New York.
- Gazdag, J. 1978. wave equation migration with the phase-shift method. *Geophysics*, **43**, 1342–1351.
- Gazdag, J., & Sguazzero, P. 1984. Migration of seismic data by phase shift plus interpolation. *Geophysics*, **49**, 124–131.

- Hörmander, L. 1985. *The analysis of linear partial differential operator*. Vol. 3. Springer-Verlag, Berlin.
- Huang, L.-J., & Wu, R.-S. 1996. 3D prestack depth migration with acoustic pseudo-screen propagators. *Pages 40–51 of: Hassanzadeh, S. (ed), Mathematical Methods in Geophysical Imaging IV*. Proc. SPIE 2822.
- Huang, L.-J., Fehler, M.C., & Wu, R.-S. 1998. Extended local Born Fourier migration method. *submitted to Geophysics*.
- Huygens, C. 1690. *traité de la lumière*. Pierre van der Aa, Leyden.
- Knepp, D.L. 1983. Multiple phase screen calculation of the temporal behavior of stochastic waves. *Proc. IEEE*, **71**, 722–737.
- Le Rousseau, J.H., & De Hoop, M.V. 1999. Scalar generalized-screen algorithms in transversely isotropic media with a vertical symmetry axis. *Geophysics, submitted*.
- Martin, J.M., & Flatté, S.M. 1988. Intensity images and statistics from numerical simulation of wave propagation in 3-D random media. *Appl. Opt.*, **27**, 2111–2125.
- Mercier, R.P. 1962. Diffraction by a screen causing large random phase fluctuations. *Proc. Cambridge Philos. Soc.*, **58**, 382–400.
- Ratcliffe, J.A. 1956. Some aspects of diffraction theory and their application to the ionosphere. *Rep. Prog. Phys.*, **19**, 190–263.
- Schulman, L.S. 1981. *Techniques and Applications of path integration*. John Wiley and Sons, New York.
- Schwartz, L. 1966. *Théorie des distributions*. 2nd edn. Hermann, Paris.

- Stoffa, P. L., Fokkema, R. M., de Luna Freire, & Kessinger, W. P. 1990. Split-step Fourier Migration. *Geophysics*, **55**, 410–421.
- Thomsen, L. 1998. *personal communication*.
- Thomson, D.J., & Chapman, N.R. 1983. A wide-angle split-step algorithm for the parabolic equation. *J. Acoust. Soc. Am.*, **74**, 1848–1854.
- Treves, F. 1967. *Topological vector spaces, distributions and kernels*. Academic Press, New York.
- Treves, F. 1980. *Introduction to pseudodifferential and Fourier integral operators*. Vol. 1. Plenum Press, New York.
- Van Stralen, M.J.N., De Hoop, M.V., & Blok, H. 1998. Generalized Bremmer series with rational approximation for the scattering of waves in inhomogeneous media. *J. Acoust. Soc. Am.*, **104**(4), 1943–1963.
- Wu, R.-S. 1994. Wide-angle elastic wave one-way propagation in heterogeneous media and an elastic wave complex-screen method. *J. Geophys. Res.*, **99**, 751–766.
- Wu, R.-S., & Jin, S. 1997. Windowed GSP (generalized screen propagators) migration applied to SEG-EAEG salt model data. *Pages 1746–1749 of: 67th Ann. Mtg. Soc. Explor. Geophys., Expanded Abstracts*.

FIGURE CAPTIONS

FIG. 1. Principal parts of the generalized-screen vertical slowness; zero-order (GSP0), first-order (GSP1) and second-order (GSP2) as a function of the horizontal slowness p . Also shown is the principal part of the vertical slowness for the split-step Fourier method. The principal part of the exact vertical slowness is shown with the inner dashed curve.

FIG. 2. Taylor expansions of the principal part of the first-order generalized-screen (GSP1) vertical slowness: zero-order (split-step Fourier = GSP1,0) and second-order (GSP1,2), as a function of horizontal slowness p . The principal part of the exact vertical slowness is shown with the inner dashed curve.

FIG. 3. Wavefronts in a constant-perturbation medium associated with the various generalized-screen approximations: second-order (GSP2), first-order (GSP1) and split-step Fourier; top: as calculated as polar reciprocal of the slowness surface; the exact and background wavefronts are shown dashed; bottom: numerical wavefront.

FIG. 4. 3D wavefield snapshots in a constant-perturbation medium associated with the various generalized screen approximations: fourth-order (GSP4), third-order (GSP3), second-order (GSP2), first-order (GSP1), and split-step Fourier. The exact wavefield is shown dashed.

FIG. 5. Top: Principal parts of the generalized-screen reflection symbols: first-order (GSR1) and second-order (GSR2) as a function of horizontal slowness p . The principal part of the exact symbol is shown dashed. Bottom: relative error of the first-order and second-order

GS approximations.

FIG. 6. Part of the Marmousi wave speed model used to generate the snapshots of Figure 7, Figure 9 and Figure 10 to Figure 14. The star locates the position of the source.

FIG. 7. Snapshot of the wavefield at time $t = 0.95$ s computed with the second order of the generalized-screen method, with no contour deformation. Figure 6 shows the wave speed model used and the source location.

FIG. 8. Applied contour deformation.

FIG. 9. Snapshot of the wavefield at time $t = 0.95$ s with the second order of the generalized-screen method. The complex contour deformation shown in Figure 8 is applied.

FIG. 10. Snapshot of the wavefield at time $t = 0.95$ s with the full two-way acoustic wave equation.

FIG. 11. Snapshot of the wavefield at time $t = 0.95$ s with the split-step Fourier method.

FIG. 12. Snapshot of the wavefield at time $t = 0.95$ s with the phase-shift-plus-interpolation method (PSPI).

FIG. 13. Snapshot of the wavefield at time $t = 0.95$ s with the fourth order of the generalized-screen method.

FIG. 14. Snapshot of the wavefield at time $t = 0.95$ s with the fourth order of the generalized-screen modeling the three first terms of the Bremmer series.

FIG. 15. Vertical profiles across the center of the SEG-EAGE salt model. The asterisk locates the position of the source; the dashed line indicates the region detailed in Figure 16 through 20.

FIG. 16. Snapshot of the wavefield at time $t = 1.2$ s with the second order of the generalized-screen method; in-line section. The three horizontal dashed lines represent the depth location of the horizontal sections of figures 18 through 20.

FIG. 17. Snapshot of the wavefield at time $t = 1.2$ s with the second order of the generalized-screen method; cross-line section.

FIG. 18. Snapshot of the wavefield at time $t = 1.2$ s with the second order of the generalized-screen method; horizontal section at depth 1500 m. The dashed lines represent the vertical sections as shown in figures 16 and 17.

FIG. 19. Snapshot of the wavefield at time $t = 1.2$ s with the second order of the generalized-screen method; horizontal section at depth 1000 m. The dashed lines represent the vertical sections as shown in figures 16 and 17.

FIG. 20. Snapshot of the wavefield at time $t = 1.2$ s with the second order of the generalized-screen method; horizontal section at depth 500 m. The dashed lines represent the vertical sections as shown in figures 16 and 17.

FIG. 21. Top: model having reflectors with dips of 0° , 15° , 30° , 45° , 60° and 75° . Middle: migration of the modeled data with split-step Fourier method. Bottom: migration of the fourth-order generalized-screen method (GSP 4).

FIG. 22. Marmousi wave speed model.

FIG. 23. Prestack depth migration of the Marmousi data with the split-step Fourier method; highlighted are features where larger difference in accuracy as compared with the result in Figure 24 can be observed.

FIG. 24. Prestack depth migration of the Marmousi data with the second-order generalized-screen method; highlighted are features where larger difference in accuracy as compared with the result in Figure 23 can be observed.

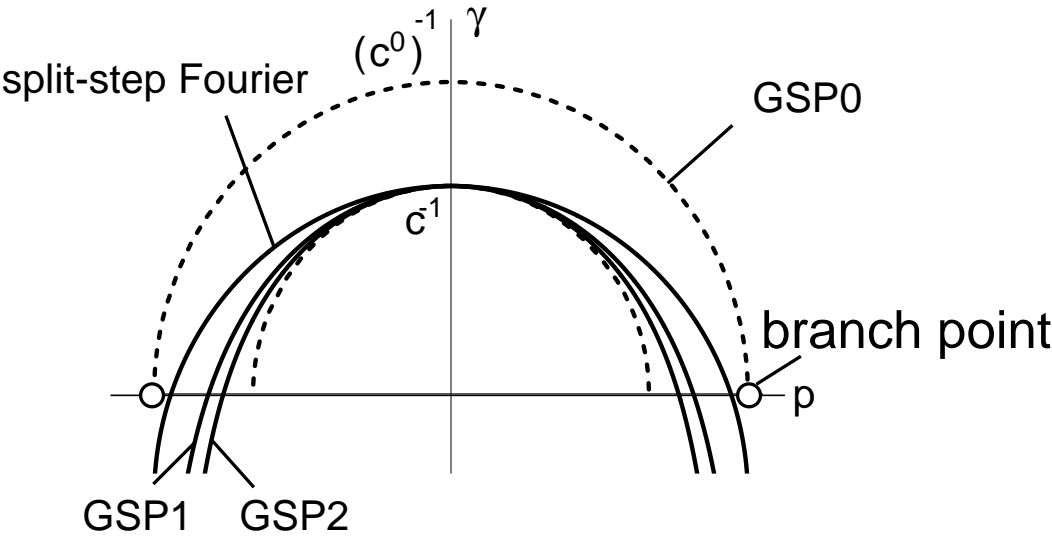


FIG. 1.

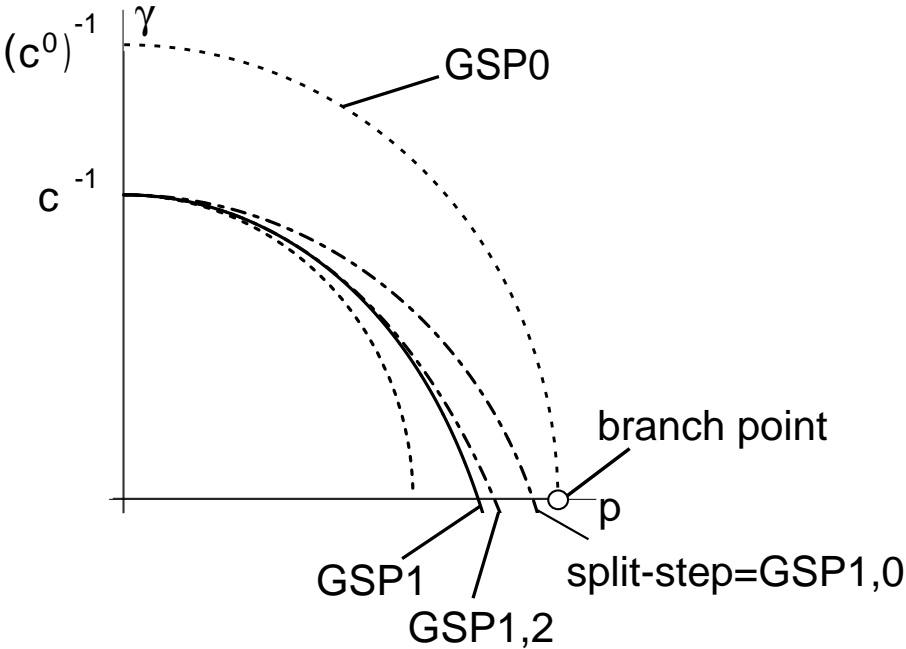


FIG. 2.

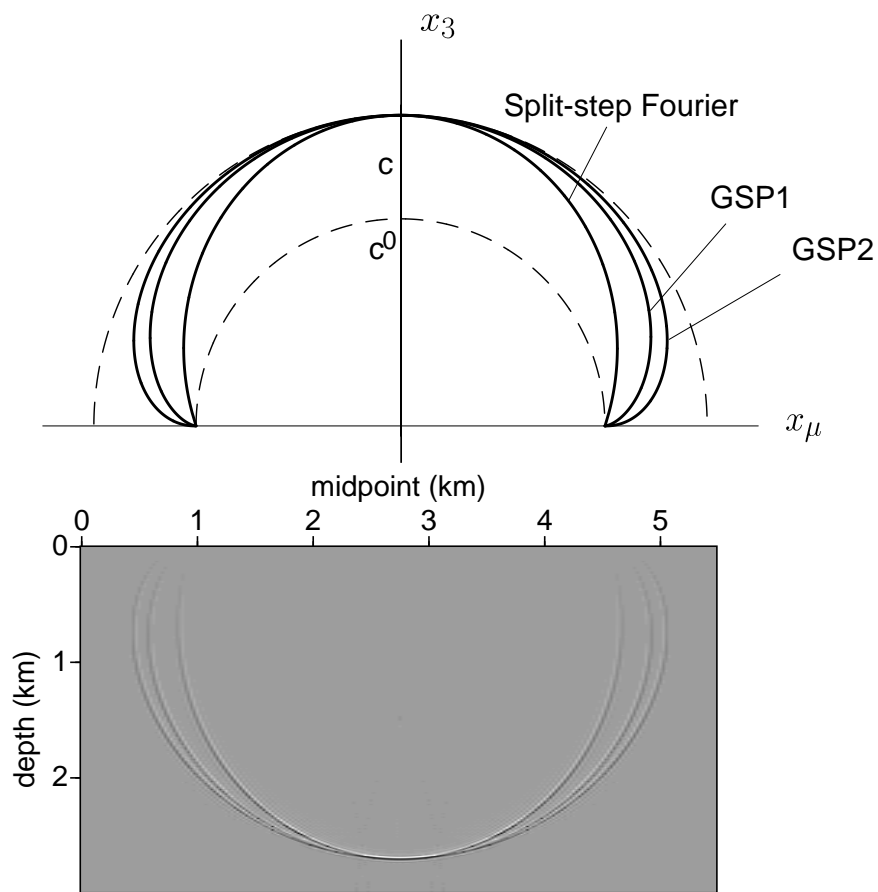


FIG. 3.

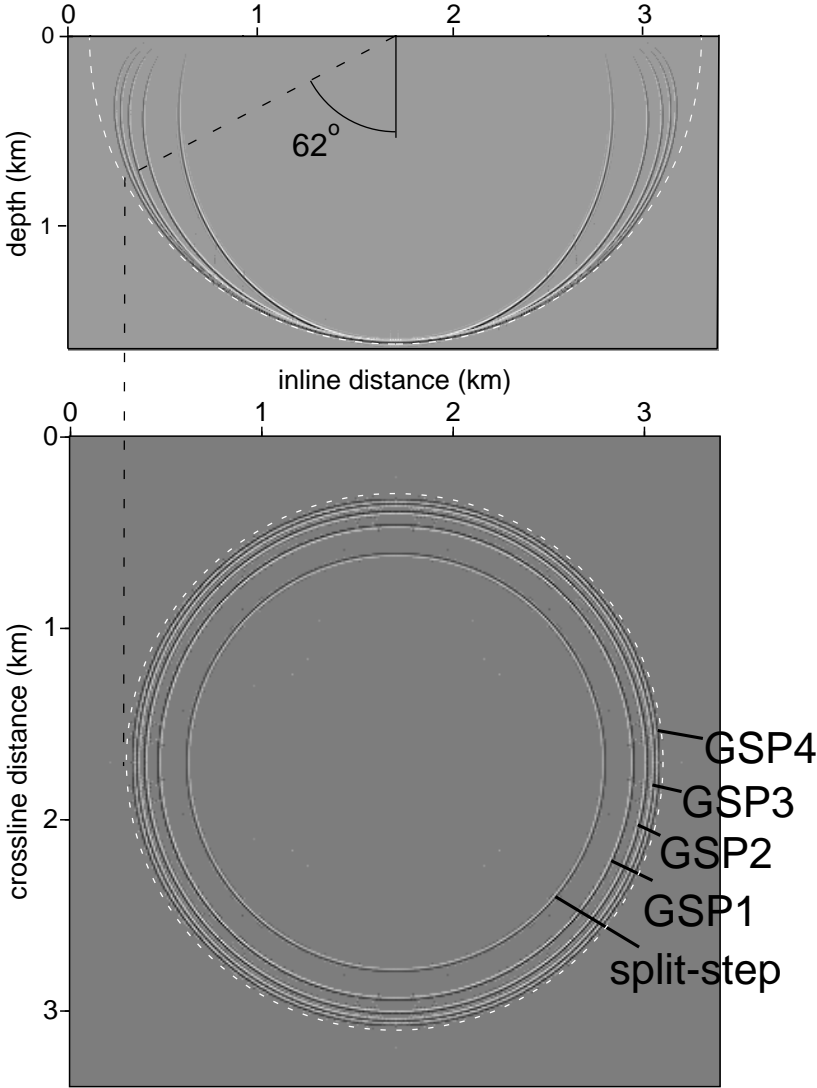


FIG. 4.

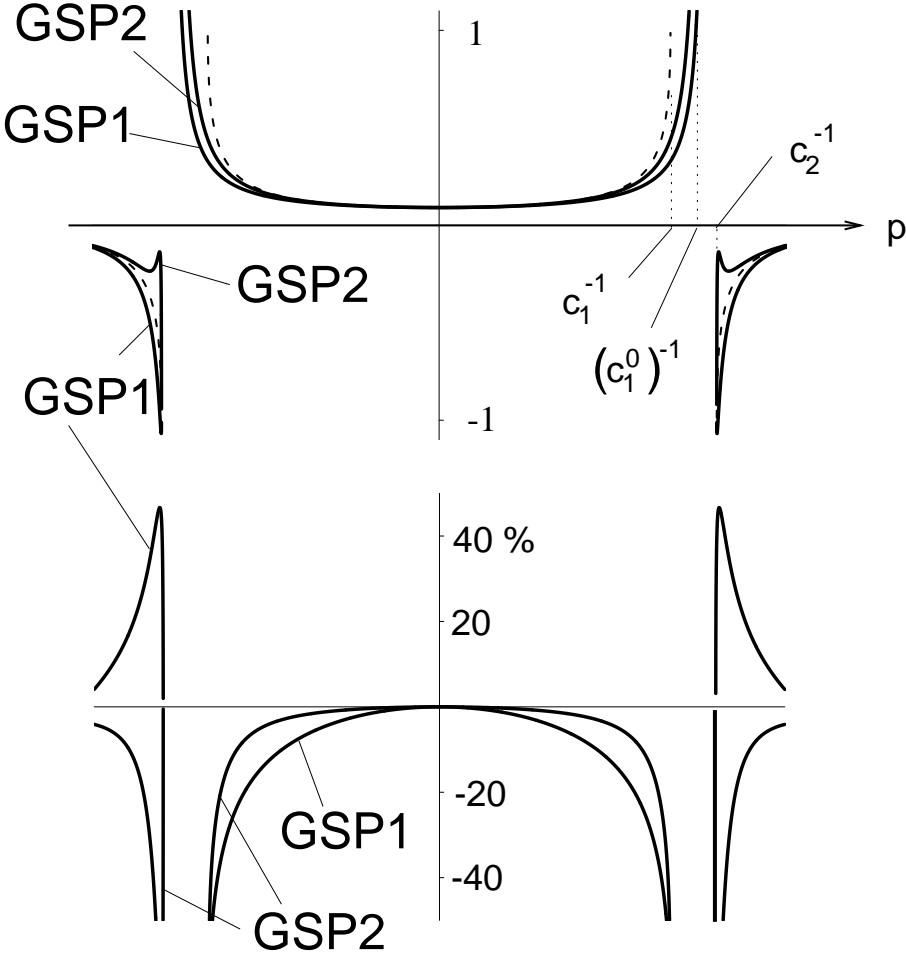


FIG. 5.

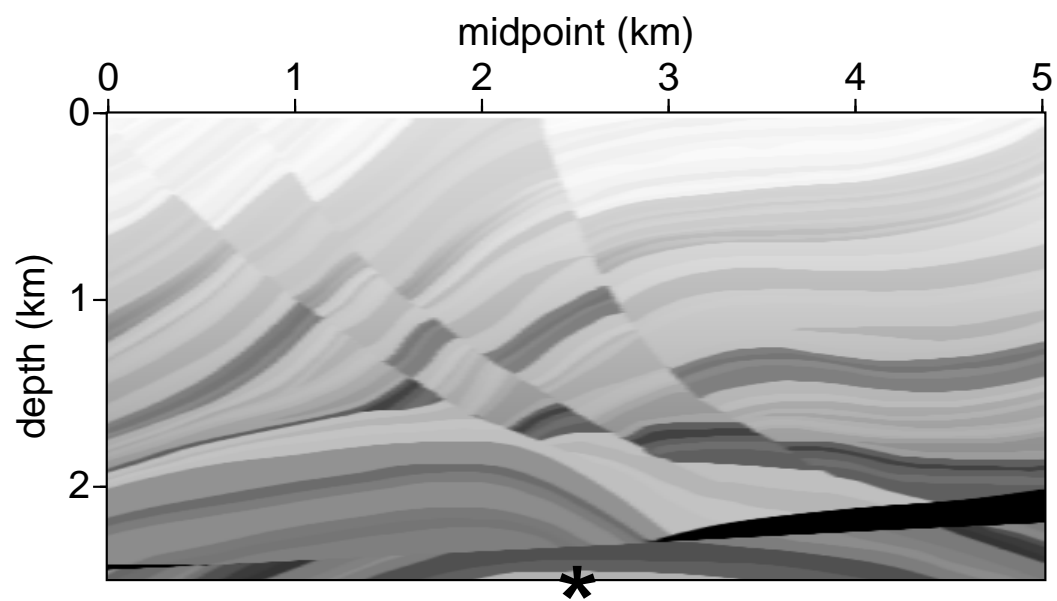


FIG. 6.

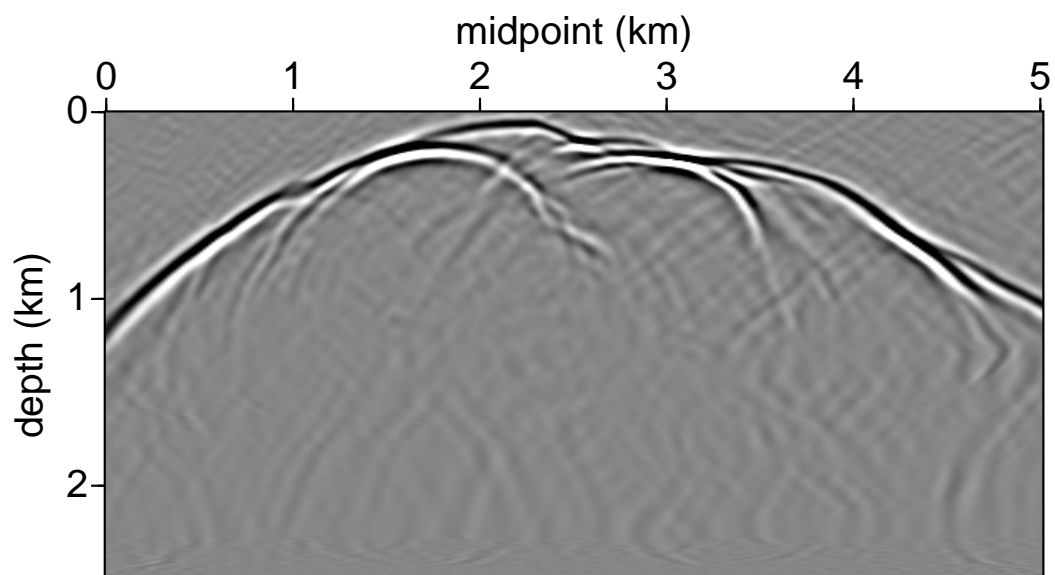


FIG. 7.

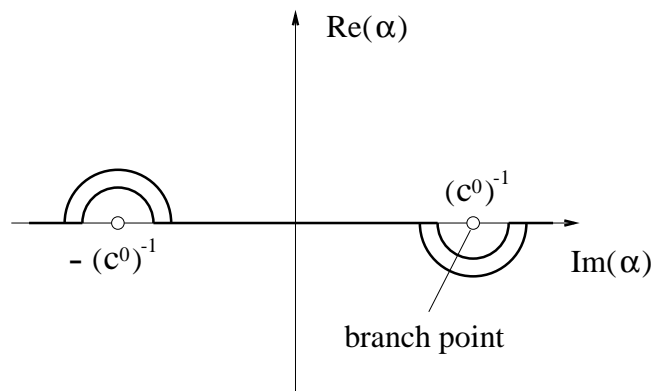


FIG. 8.

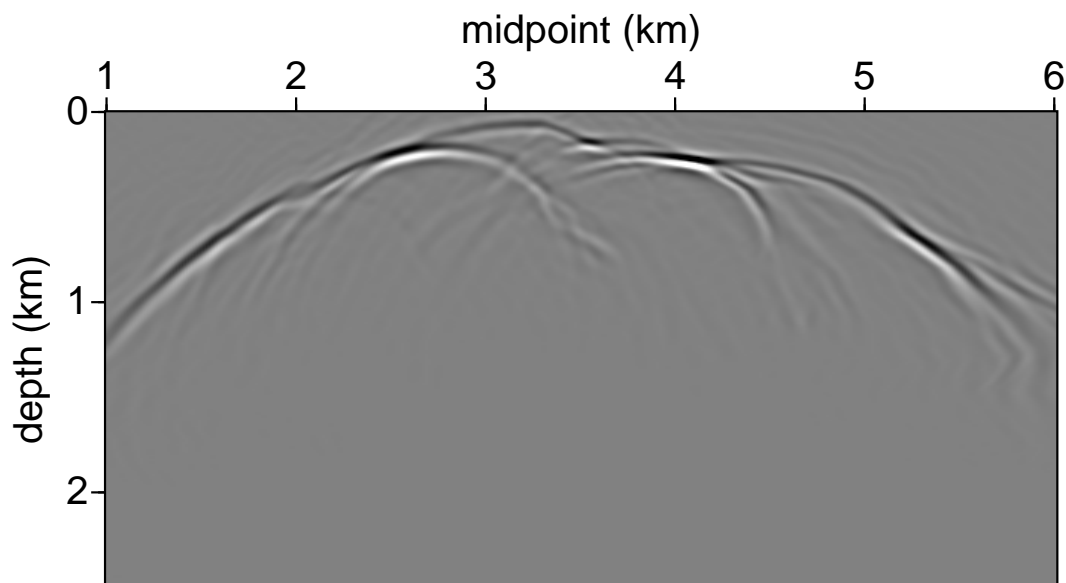


FIG. 9.

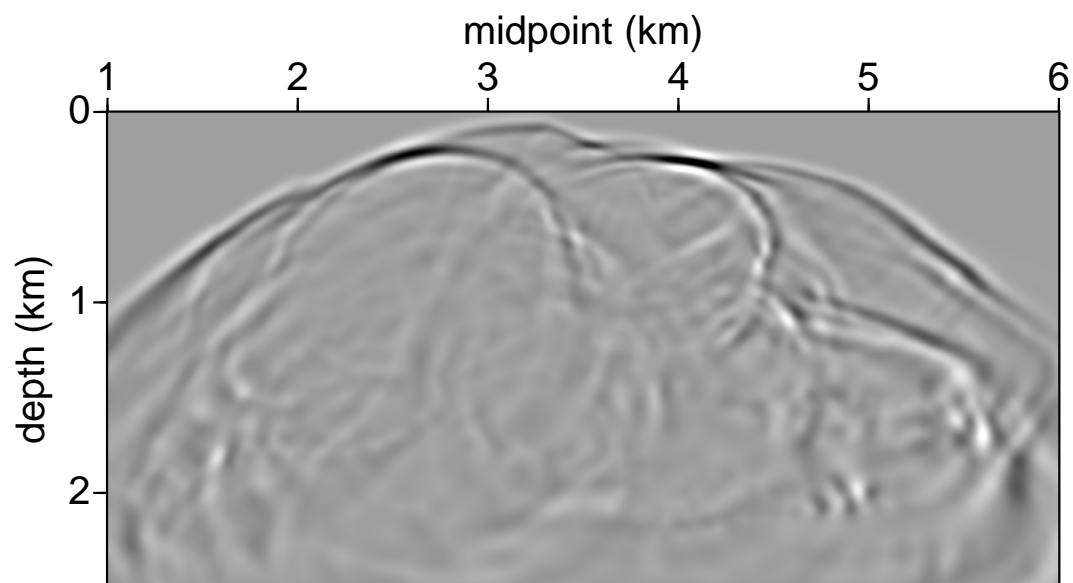


FIG. 10.

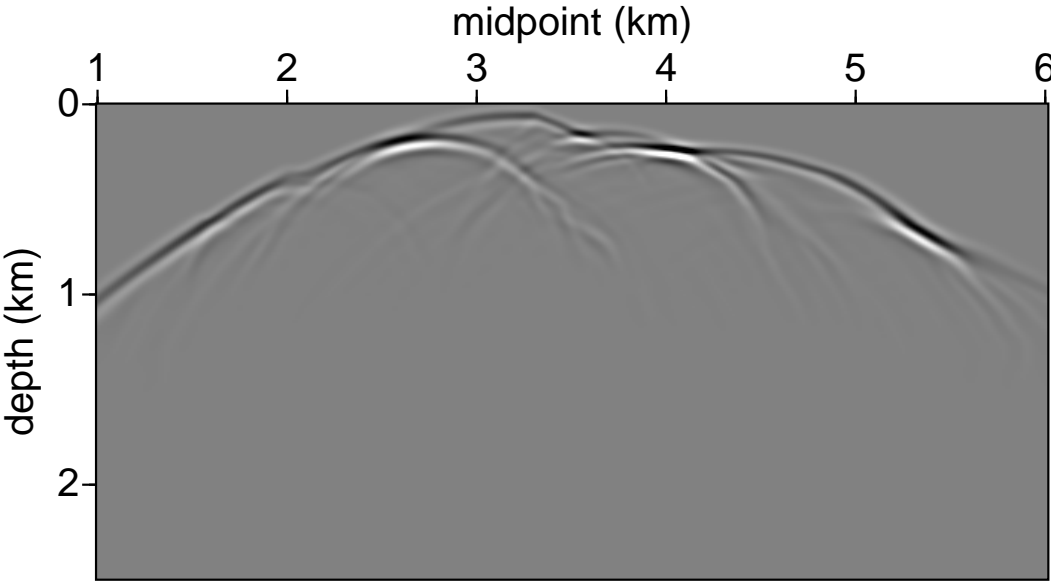


FIG. 11.

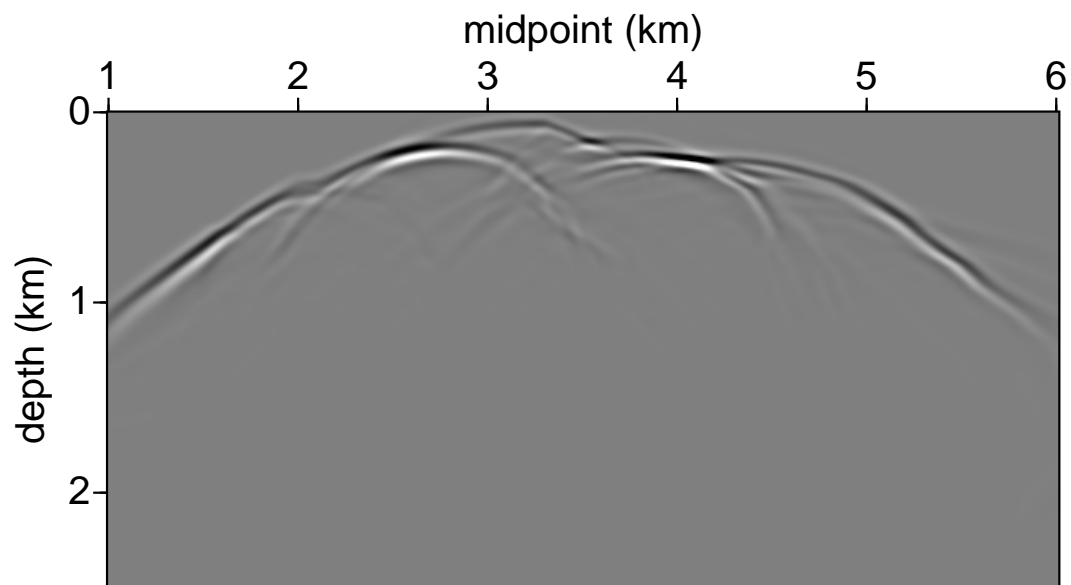


FIG. 12.

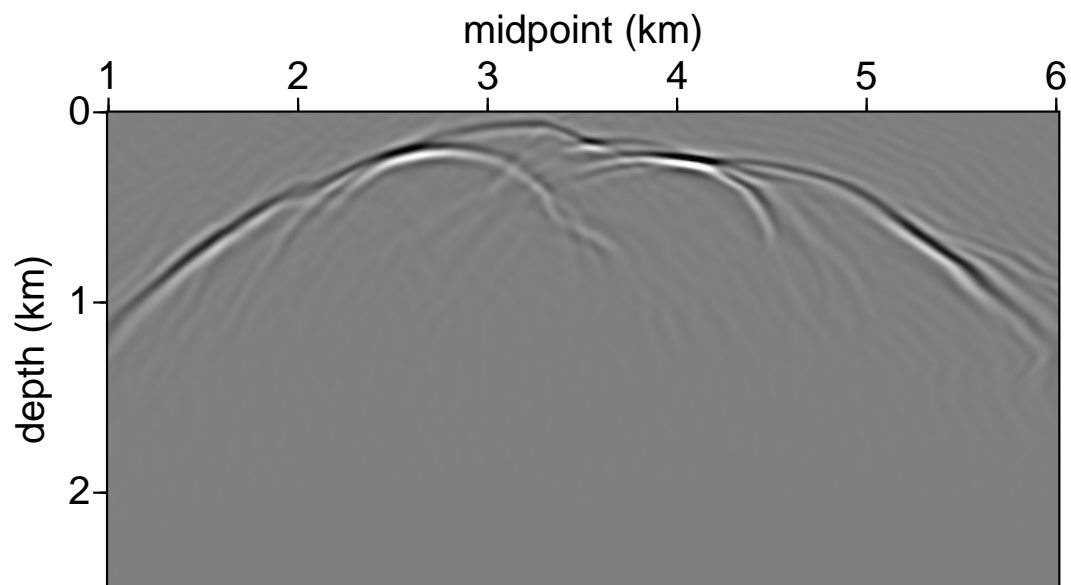


FIG. 13.

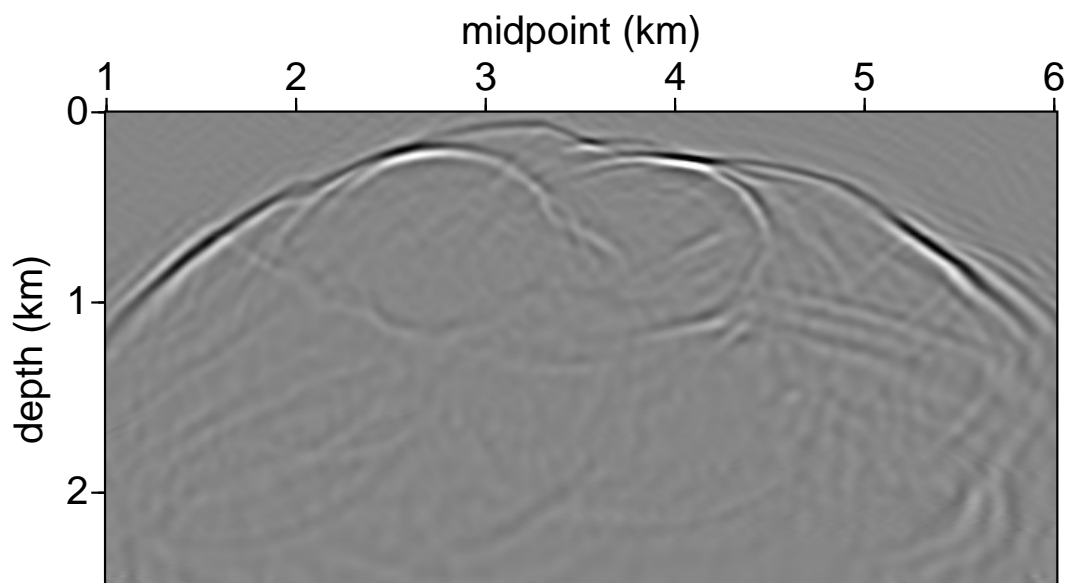


FIG. 14.

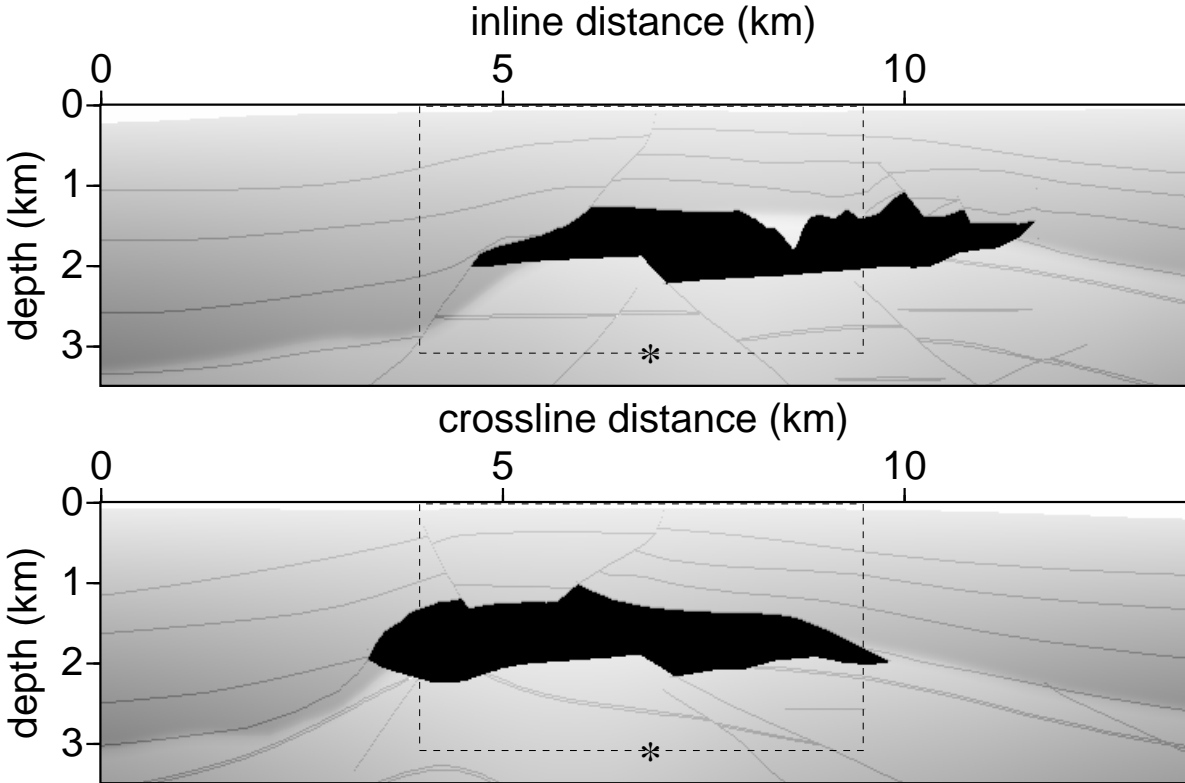


FIG. 15.



FIG. 16.

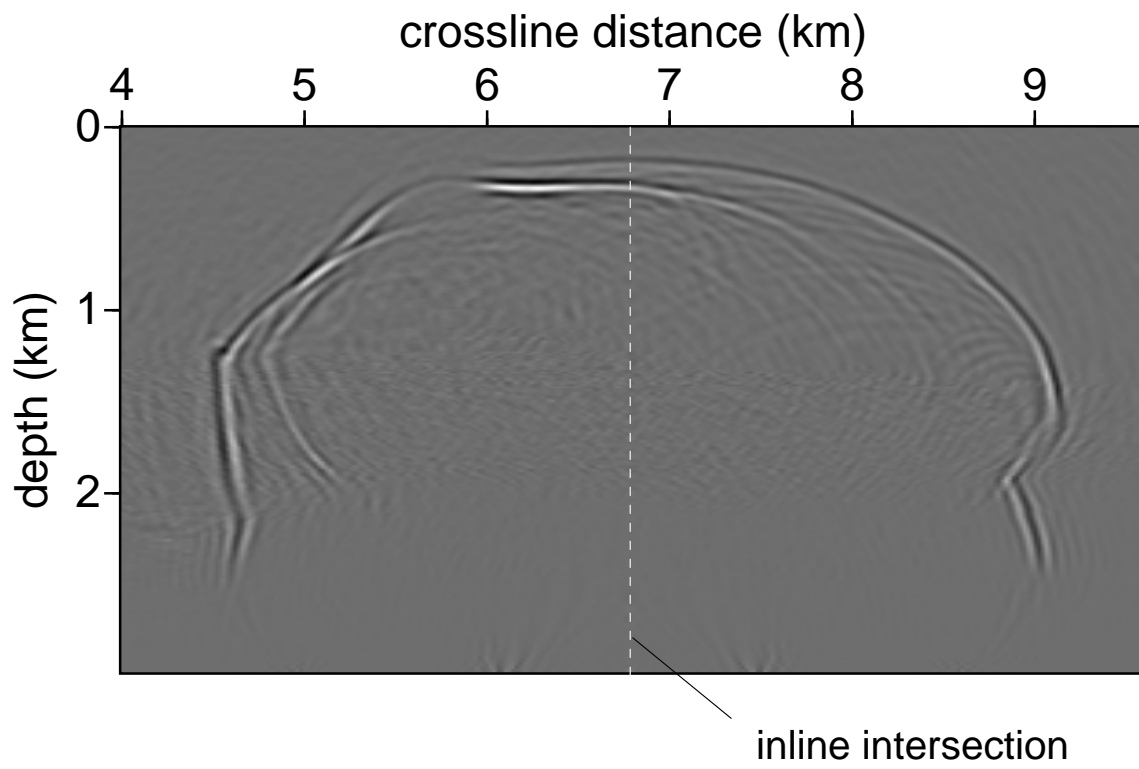


FIG. 17.

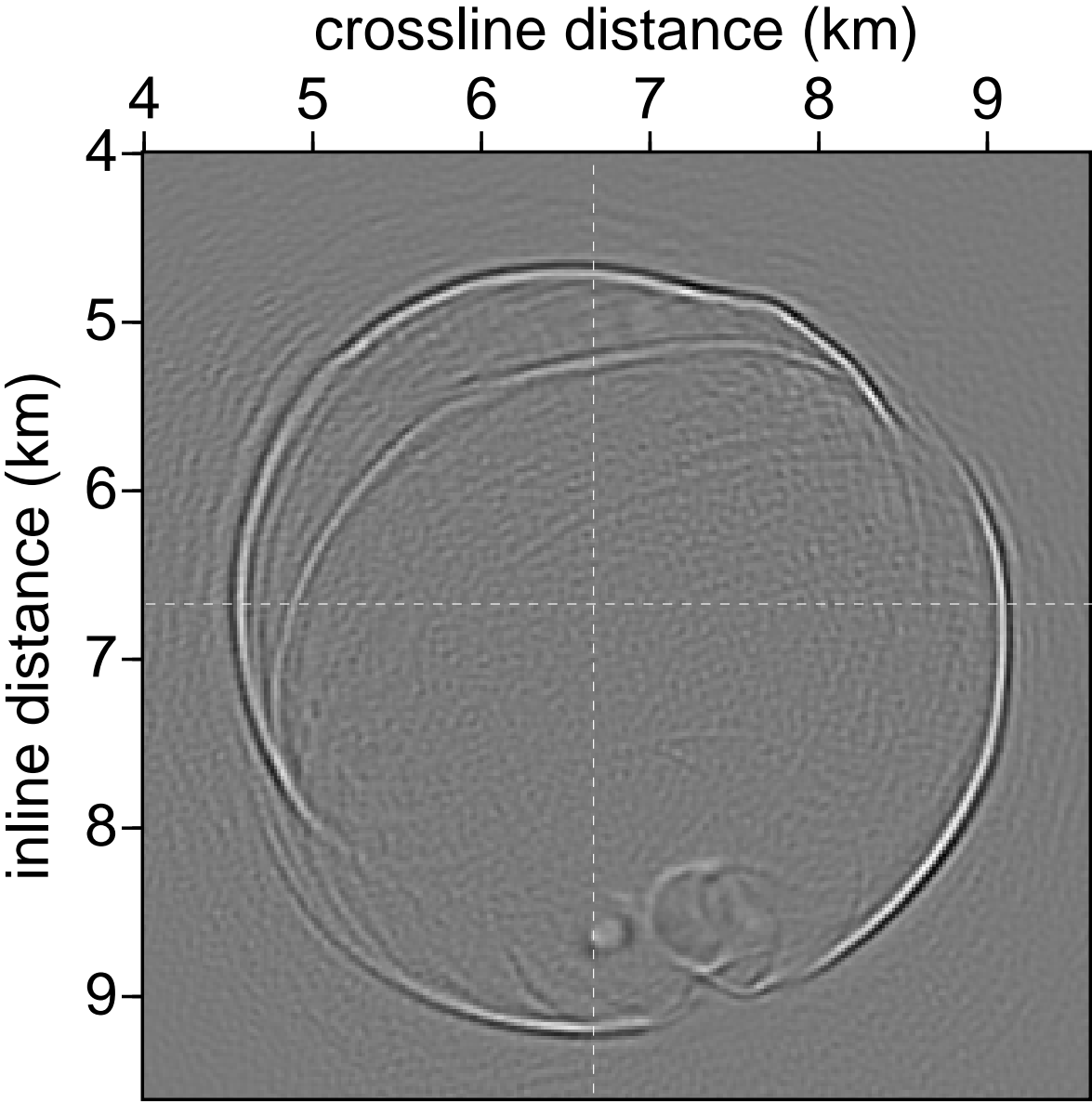


FIG. 18.

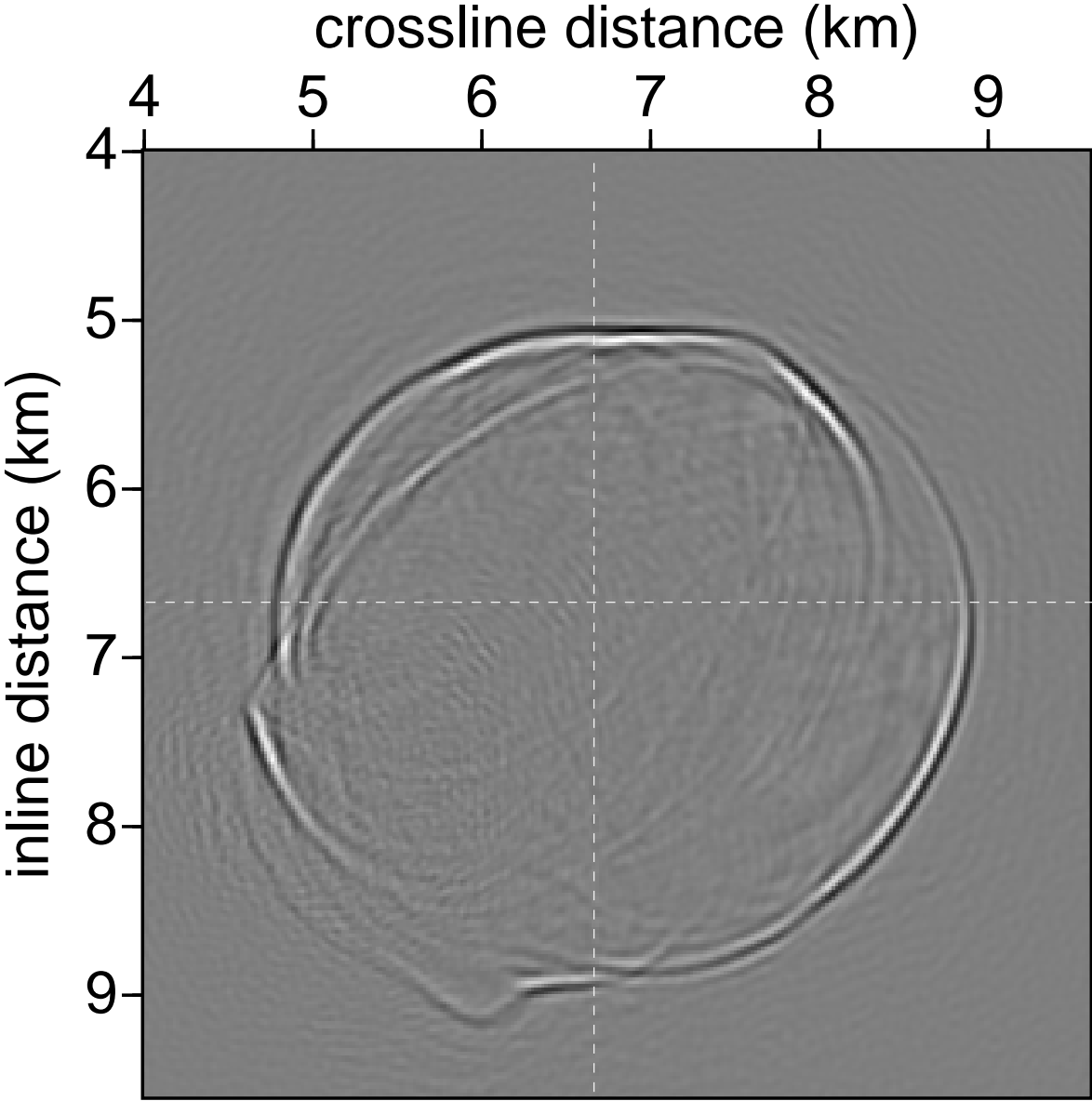


FIG. 19.

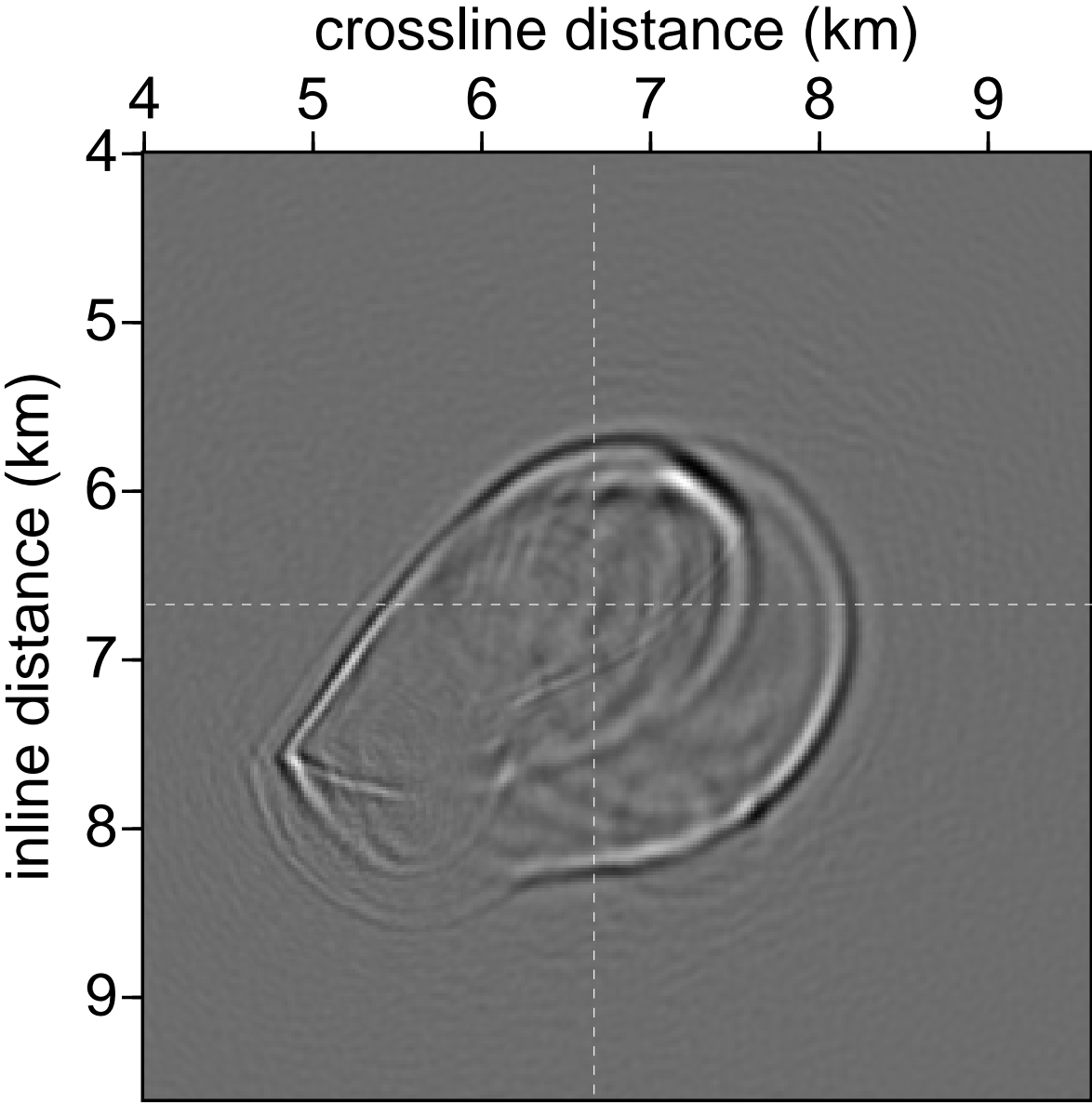


FIG. 20.

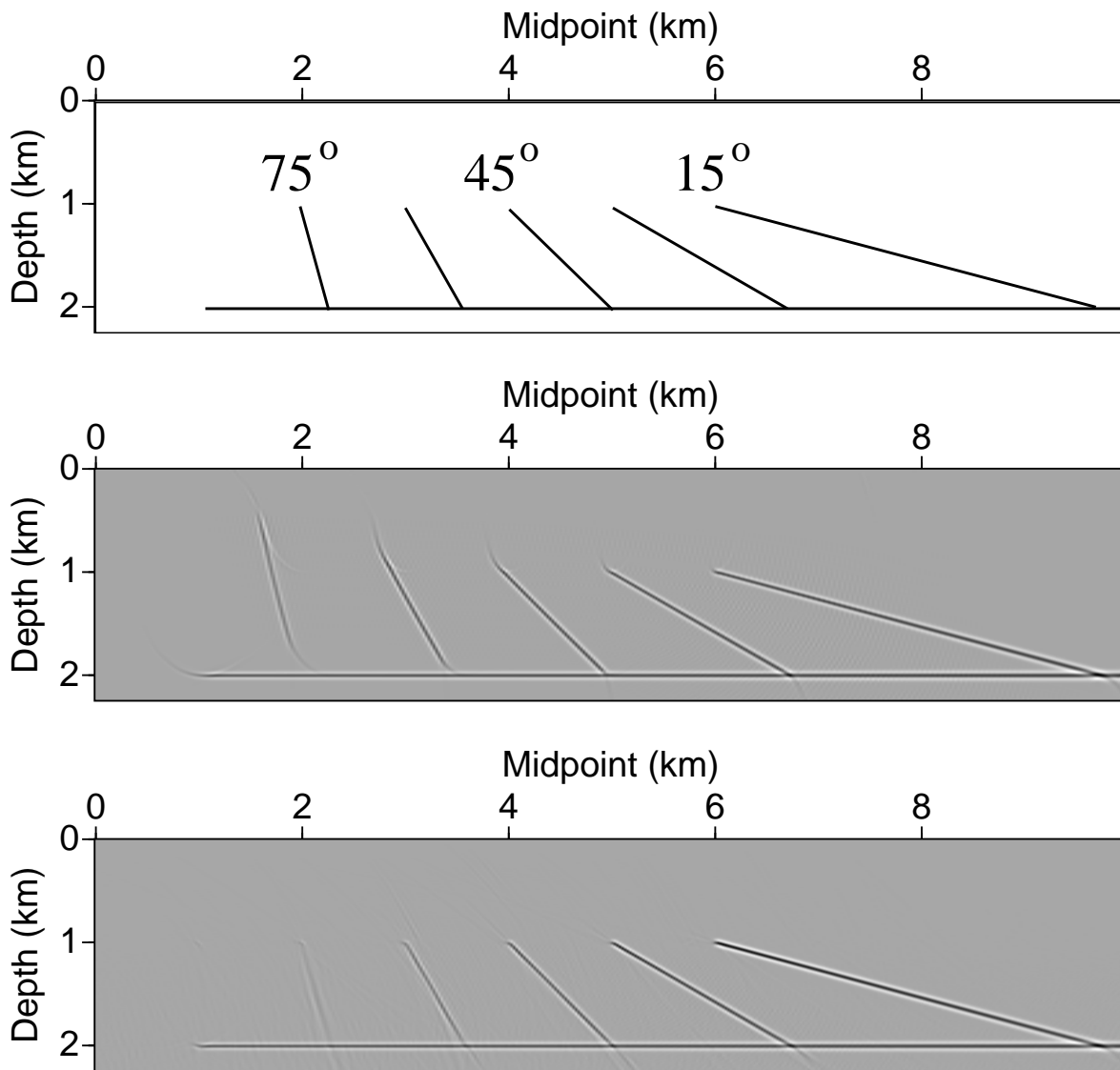


FIG. 21.

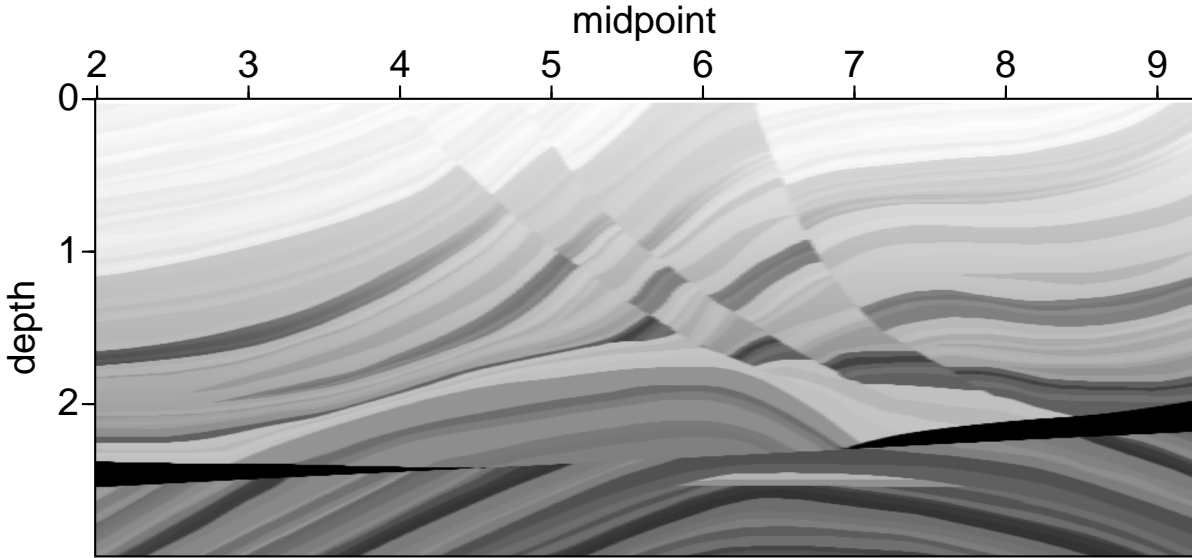


FIG. 22.

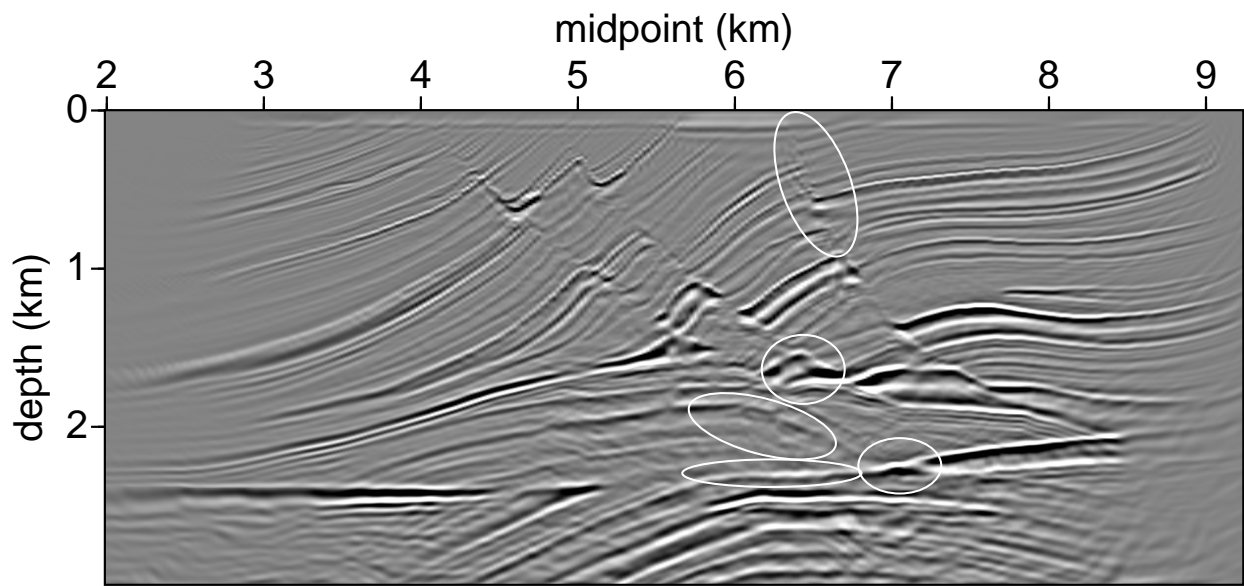


FIG. 23.

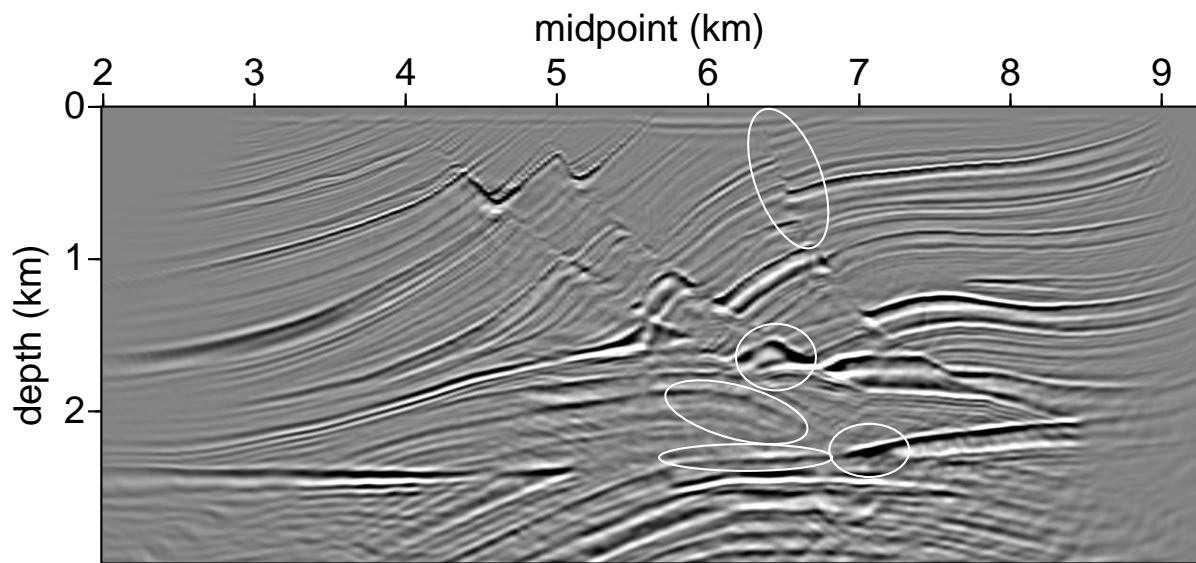


FIG. 24.

APPENDIX A: RELATIONSHIP BETWEEN ONE-WAY GREEN'S FUNCTION AND PROPAGATOR

The propagator, $g^{(\pm)}$, associated with the one-way wave equation satisfies the pseudodifferential equation

$$[\partial_3 \pm s\Gamma] g^{(\pm)}(x_\mu, x_3; x'_\nu, x'_3) = 0, \quad (\text{A-1})$$

complemented with the initial condition

$$g^{(\pm)}(x_\mu, x_3 = x'_3; x'_\nu, x'_3) = \delta(x_\mu - x'_\nu). \quad (\text{A-2})$$

Let us consider a function $\phi(x_\mu, x_3)$ that satisfies the one-way wave equation also. With properties (A-1) and (A-2), we have

$$\phi(x_\mu, x_3) = \int dx'_1 dx'_2 g^{(\pm)}(x_\mu, x_3; x'_\nu, x'_3) \phi(x'_\nu, x'_3), \quad (\text{A-3})$$

hence the terminology propagator. We now prove that the function $\mathcal{G}^{(\pm)}(x_\mu, x_3; x'_\nu, x'_3)$ defined as

$$\mathcal{G}^{(\pm)}(x_\mu, x_3; x'_\nu, x'_3) = \pm H(\pm[x_3 - x'_3]) g^{(\pm)}(x_\mu, x_3; x'_\nu, x'_3), \quad (\text{A-4})$$

is a Green's function associated with the one-way wave equation. H is the Heaviside function.

Applying the one-way operator to expression (A-4) yields

$$\begin{aligned} [\partial_3 \pm s\Gamma] \mathcal{G}^{(\pm)}(x_\mu, x_3; x'_\nu, x'_3) &= \pm g^{(\pm)}(x_\mu, x_3; x'_\nu, x'_3) \partial_3 H(\pm[x_3 - x'_3]) \\ &\quad \pm H(\pm[x_3 - x'_3]) [\partial_3 \pm s\Gamma] g^{(\pm)}(x_\mu, x_3; x'_\nu, x'_3). \end{aligned} \quad (\text{A-5})$$

The second term in equation (A-5) vanishes because of property (A-1), hence

$$\begin{aligned} [\partial_3 \pm s\Gamma] \mathcal{G}^{(\pm)}(x_\mu, x_3; x'_\nu, x'_3) &= \pm g^{(\pm)}(x_\mu, x_3; x'_\nu, x'_3) [\pm\delta(x_3 - x'_3)] \\ &= g^{(\pm)}(x_\mu, x_3 = x'_3; x'_\nu, x'_3) \delta(x_3 - x'_3) \\ &= \delta(x_\mu - x'_\nu) \delta(x_3 - x'_3), \end{aligned} \quad (\text{A-6})$$

which is the defining equation for the one-way Green's function. The occurrence of the Heaviside function, enforces the Green's function to be causal; the propagator is not.

In this paper, we define a one-way Green's function with respect to the preferred spatial direction (x_3). In the field of Quantum mechanics, the same arguments are used to define the one-way Green's function in time using the propagator that satisfies the Schrödinger equation (Cohen-Tannoudji *et al.*, 1977).

APPENDIX B: REDUCTION TO THE PRINCIPAL PARTS

Using the composition rule for symbols of pseudodifferential operators (Treves, 1980), the operator equation,

$$\Gamma^2 = A , \tag{B-1}$$

is transformed into an equation for the corresponding left symbols (De Hoop, 1996):

$$\exp \left[-i \partial_{\alpha'_\sigma} D_{x'_\sigma} \right] \gamma(x_\mu; \alpha'_\sigma) \gamma(x'_\sigma; \alpha_\nu) \Big|_{(x'_\mu, \alpha'_\nu) = (x_\mu, \alpha_\nu)} = a(x_\mu; \alpha_\nu) , \tag{B-2}$$

where γ is the left symbol of Γ and a is the left symbol of A , i.e.,

$$\Gamma(x_\mu, x_3; D_\nu) \exp(i s \alpha_\sigma x_\sigma) \equiv \gamma(x_\mu, x_3; \alpha_\nu) \exp(i s \alpha_\sigma x_\sigma) ,$$

$$A(x_\mu, x_3; D_\nu) \exp(+i s \alpha_\sigma x_\sigma) \equiv a(x_\mu, x_3; \alpha_\nu) \exp(+i s \alpha_\sigma x_\sigma) .$$

From the form of A in the acoustic-pressure-normalization analog of equation (4) (De Hoop, 1996) we have

$$a = \kappa \rho + \alpha_\nu \alpha_\nu - \rho^{-1} (D_\nu \rho) i \alpha_\nu - \rho^{-1} (D_\nu D_\nu \rho) - \rho^{-2} (D_\nu \rho) (D_\nu \rho) . \tag{B-3}$$

As $\omega \rightarrow \infty$ the composition of symbols tends to an ordinary multiplication, and the solution of equation (B-2) reduces to the principal parts, γ_1 and a_2 respectively, of the symbols:

$$\gamma_1(x_\mu; \alpha_\nu) \gamma_1(x_\mu; \alpha_\nu) = a_2 = \kappa \rho + \alpha_\nu \alpha_\nu = c^{-2} + \alpha_\nu \alpha_\nu . \tag{B-4}$$

Referring to the contrast formulation made here and in De Hoop *et al.* (1999), the ‘high-frequency’ approximation of equation (B-4) can also be expressed by assuming that the vertical-slowness symbol depends only on the magnitude (ϵ) of the medium perturbation, but not on the smoothness (Ω) of the medium perturbation, i.e. γ_1 is $\mathcal{O}(\Omega^0)$.